MEASUREMENT OF THE LOW ENERGY NUCLEAR RESPONSE IN NaI(Tl)

CRYSTALS FOR USE IN DARK MATTER DIRECT DETECTION EXPERIMENTS

A Dissertation

by

TYANA MICHELE STIEGLER

Submitted to the Office of Graduate Studies of
Texas A&M University
in partial fulfillment of the requirements for the degree of

DOCTOR OF PHILOSOPHY

Chair of Committee,	Robert C. Webb, Sr.
Committee Members,	Bhaskar Dutta
	Saskia Mioduszewski
	Leslie A. Braby
Head of Department,	George R. Welch

August 2013

Major Subject: Physics

ABSTRACT

The response of low energy nuclear recoil in NaI(Tl) is investigated in the following experiment. Such detectors have been used recently to search for evidence of dark matter in the form of weakly interacting massive particles (WIMPs). NaI(Tl) crystal response to nuclear recoil energy deposition is a key element in these searches. I discuss the cosmological and experimental motivations for these experiments, followed by an overview of the physics of direct detection and current relevant WIMP search experiments.

With the experiment motivations covered, the details of NaI(Tl) detectors are reviewed. The specifics of our experiment are laid out including the neutron production, neutron beam calibration, shielding optimization, experimental design and setup. Then the crystal response calibration studies and Geant4 simulations are discussed followed by the final quenching factor values and uncertainties.

This experiment measured quenching factors for sodium recoils in the energy range of (9 keV-40 keV) of 19%-27% QF. These results are similar to current published measurements. Interesting features of the QF measurements include an increase at low energies and a dip in the values at 30 keV, the iodine K-shell absorption edge. The goal of this experiment was to add valuable measurements of nuclear recoils at low energies that are relevant to low-mass WIMP experiments. Future plans will improve and expand on these measurements in order to better understand the response of NaI(Tl) at low energies.

DEDICATION

for my father

ACKNOWLEDGEMENTS

through graduate school with me and loved me anyway, without you I would never have made it through this. Thank you for being the love of my life. Finally, I'd like to thank my mother. She never wavered in her love and support, my inspiration and my hero, now and always.

NOMENCLATURE

DM	Dark Matter
WIMP	Weakly Interacting Massive Particle
CDM	Cold Dark Matter
keVee	Electron equivalent energy of nuclear recoil
keVnr	Nuclear recoil energy
QF	Quenching Factor
PMT	Photomultiplier Tube
NaI(Tl)	Thallium doped sodium iodide
CMB	Cosmic Microwave Background
FLRW	Friedmann-Lemaître-Robertson-Walker
HI	Atomic Hydrogen
WMAP	Wilkinson Microwave Anisotropy Probe
ISW	Integrated Sachs-Wolfe
SDSS	Sloan Digital Sky Survey
LRG	Luminous Red Galaxies
BAO	Baryonic Acoustic Oscillation
CERN	European Organization for Nuclear research (*Conseil Européen pour la Recherche Nucléaire)*
BBN	Big-Bang Nucleosynthesis
ADMX	Axion Dark Matter Experiment

CAST	CERN Axion Solar Telescope
SUSY	Supersymmetry
LSP	Lightest Supersymmetric Particle
MSSM	Minimal Supersymmetric Model
C.L.	Confidence Level
SI	Spin-Independent
SD	Spin-Dependent
PVD	Physical Vapor Deposition
spe	Single Photoelectron
nPR	Non-proportional Response
DAQ	Data Acquisition System
FWHM	Full Width Half Maximum
EC	Electron Capture

TABLE OF CONTENTS

LIST OF FIGURES

LIST OF TABLES

1. INTRODUCTION

Beginning with F. Zwicky in 1933 [1], physicists have been faced with the experimental fact that the Universe is missing a considerable fraction of its total mass. Numerous experiments and astronomical observations in the intervening years have pointed to the astounding conclusion, that the majority of the energy density in the Universe is not the galaxies, stars, and gas clouds that we observe. We instead see a mix of unseen dark matter and dark energy, like separate pieces in the puzzle that is our universe. The "Dark Matter", as it has been termed, does not emit, absorb, or scatter light. Up to now Dark Matter has been detected only through its interactions via the gravitational force. This has left scientists with the longstanding problem of what exactly is the nature of this Dark Matter.

The first observations of Dark Matter were of the gravitational interaction of various astronomical bodies, the rotational speed of stars and galaxies, and the orbital velocity of galaxies in clusters. More recently the evidence was increased by observations of the anisotropies in the Cosmic Microwave Background (CMB), the large scale distribution of matter in the Universe and gravitational lensing of objects by galaxy clusters. In order to fully understand the implications of the cosmological evidence for Dark Matter it is necessary to first setup a preliminary framework that quantifies the density of the Universe as well as several other parameters. To that end, the next section will review several important cosmological definitions and equations in order to better explain the current astronomical evidence for non-relativistic, non-baryonic Dark Matter. After reviewing the theoretical background, the ΛCDM model of the Universe will be

discussed along with the current observations associated with it. Followed by a look at possible Dark Matter candidates, from which the weakly interacting massive particle or WIMP emerges as the most likely candidate to solve the missing mass problem in our Universe.

1.1 Dark Matter: Theoretical Overview

This section lays out a short explanation of the theories that give us the mass density of the Universe and the nature of its components. The goal being to illuminate the types of matter that make up the Universe and how much of it is non-baryonic Dark Matter. A more detailed discussion of the following concepts can be found for example in [2].

It is instructive to start with Einstein's field equations. The field equations describe the curvature of space-time due to the presence of matter. The curvature is quantified by the metric tensor, $g_{\mu\nu}$. It is used to calculate the distance between two points in space

$$ds^2 = g_{\mu\nu}dx^\mu dx^\nu \tag{1.1}$$

The metric tensor is the dynamic variable in the Einstein field equations

$$R_{\mu\nu} - \frac{1}{2}g_{\mu\nu}R = \frac{8\pi G}{c^4}T_{\mu\nu} + g_{\mu\nu}\Lambda \tag{1.2}$$

where $R_{\mu\nu}$ and R are the Ricci tensor and scalar respectively, constructed from the second derivatives of the metric tensor, $g_{\mu\nu}$. G is Newton's- gravitational constant. The energy-momentum tensor of the medium is $T_{\mu\nu}$ and Λ is the cosmological constant. The

indices μ and ν each have one time component and three space components, giving a total of 16 separate equations. The symmetry of $g_{\mu\nu}$ eliminates some of those, leaving 10 independent, non-linear, coupled differential equations.

In order to further simplify the situation the cosmological principle can be invoked. It states that at large distances the Universe appears homogeneous and isotropic. With these two assumptions we can use the Friedmann-Lemaître-Robertson-Walker metric (FLRW) to solve the field equations. Using this metric the invariant line element becomes

$$ds^2 = c^2 dt^2 - a(t)^2 \left[\frac{dr^2}{(1 - kr^2)} + r^2 d\Omega^2 \right] \tag{1.3}$$

The line element is expressed in commoving coordinates and a(t) is the scale factor for the expansion(contraction) of the Universe. The constant, k, describes the curvature of space-time and can take the values of -1, 0, or 1 for open, flat, and closed geometries respectively. By using the FLRW metric and the ideal gas law form of the energy-momentum tensor, we can derive the Friedman equations from the Einstein field equations. The ideal gas law for the energy-momentum tensor is

$$T_{\mu\nu} = diag(-c^2 \rho, p, p, p) \tag{1.4}$$

This assumes a perfect fluid with no viscosity or heat flow where ρ is the mass density and p is the measurable pressure. Taking the time-time (00) component gives the first Friedmann equation

$$\left(\frac{1}{a} \frac{da}{dt} \right)^2 + \frac{kc^2}{a^2} = \frac{8\pi}{3c^2} G\rho + \frac{\Lambda}{3} \tag{1.5}$$

3

and the space-space (ii) component gives the second

$$\left(\frac{1}{a}\right)\frac{d^2a}{dt^2} = \frac{-4\pi G}{3c^2}(\rho + 3p) + \frac{\Lambda}{3}$$ (1.6)

Eq. 1.6 is an equation of motion that describes a dynamic Universe. When Einstein originally introduced the cosmological constant in 1915 it was to ensure a static Universe. What he later named his "greatest blunder" was to set $\Lambda = 4\pi G\rho/c^2$, so that the Universe was neither expending nor contracting. Today we use the cosmological constant to describe the accelerating expansion of the Universe. It can be understood as the vacuum energy density of the Universe and is often termed "Dark Energy".

The cosmic scale factor a(t) describes the rate of expansion(contraction) of the Universe with time. It is normalized such that a(t_0) = 1, where t_0 is the present time. Remembering that $\vec{v} = a\vec{x}$, and by definition x is a stationary position, combine this with Hubble's Law,

$$\vec{v} = H\vec{r} = cz$$ (1.7)

$$H(t) = \frac{1}{a}\frac{da}{dt}$$ (1.8)

Hubble's Law describes the recession velocity of objects with respect to their distance from us as well as the rate of expansion of the Universe with respect to time. The cosmological redshift, z, is the measurement of the increase of the wavelength of light from a distant objects due to cosmic expansion. As a photon travels from a distant object the expansion of space dilates the wavelength, making it longer and shifting it down in the spectrum. The current acceleration of the Universe can be measured by comparing the observed redshift and the distance, determined by using a standard candle reference.

Type 1a super novae are one such standard candle and will be discussed in more detail in Section 1.2.4.

The rate of expansion at the current time, t_0, is called the Hubble Constant

$$H_0 = \left(\frac{1}{a}\frac{da}{dt}\right)_{t=t_0} \tag{1.9}$$

It's current value has been measured at (69.3 km/s/Mpc)[3].

It is insightful to rewrite the 1st Friedmann equation in terms of the critical energy density, ρ_c. The total density is

$$\Omega = \sum_i \Omega_i \;\; ; \;\;\; \Omega_i(i=m,k,\Lambda) \tag{1.10}$$

The components of the total density are the matter, curvature and vacuum energy densities relative to the critical density.

$$\Omega_m = \frac{\rho_0}{\rho_c}$$
$$\Omega_k = \frac{1}{H_0^2 a_0^2 R^2} \tag{1.11}$$
$$\Omega_\Lambda = \frac{\Lambda}{3H_0^2}$$

If the curvature of the Universe and the vacuum energy density are assumed to be zero then we obtain the critical density for a flat (Euclidean) geometry.

$$\rho_c = \frac{3H_0^3}{8\pi G} \tag{1.12}$$

Rewriting the density parameters in terms of their value relative to the critical density and then substituting them into the 1st Friedmann equation gives

$$\left(\frac{H}{H_0}\right)^2 = \Omega_m\left(\frac{a_0}{a}\right)^3 + \Omega_k\left(\frac{a_0}{a}\right) + \Omega_\Lambda \qquad (1.13)$$

Recalling that $a(t_0) = a_0 = 1$ it is obvious that $\Omega_m + \Omega_k + \Omega_\Lambda = 1$ at the present time. Experiments have shown us that $\Omega_k \approx 0$, which leaves $\Omega_m + \Omega_\Lambda \approx 1$. The dark energy component is around 71%, leaving 29% for the total matter component. The mass component is made up of about 4% baryonic matter and the remaining 23% is the Dark Matter component of the density. This particular explanation is called the ΛCDM model. Where Λ represents the dark energy component, and CDM stands for Cold Dark Matter. Constraints on the matter density are obtained through analysis based on the observation of luminous matter in galaxies and galaxy clusters, gravitational lensing, and the theory of Big Bang Nucleosynthesis [4]. Exact experimental values for these parameters and the implications therein will be discussed in the next section.

1.2 Evidence for Dark Matter: Astrophysical Observations

The ΛCDM model is currently the best explanation for the state of the Universe. It is a model depending on six parameters that are constrained by observations of large scale structures, Type 1a supernovae, anisotropies in the Cosmic Microwave Background, and Big Bang Nucleosynthesis. The current goal of research in this area is to accurately measure these parameters in order to build a precise cosmological model of the Universe.
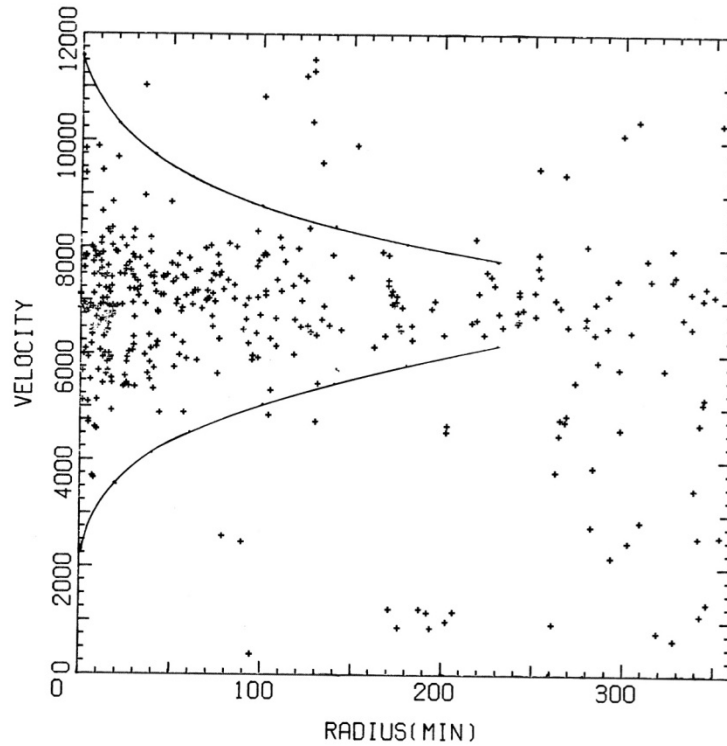
Fig. 1. Distribution of radial velocities in the Coma cluster as a function of distance from the center. The plot shows the clustering of velocities in the galaxies closest to the cluster center, It is a gravitationally bound system with the lines drawn to separate cluster members from foreground and background galaxies. The galaxies contained in the cluster are clear out to 3-4°. Zwickey used the velocities of eight of the galaxies to estimate the cluster mass at 170x the mass calculated from the luminosity alone. (Fig. from [5])

1.2.1 Cluster Redshift Measurements

The first speculations about an unseen matter component in the Universe were made by Fritz Zwicky in 1933. He published a paper on the velocity distribution of galaxies in the Coma cluster [1]. In it he calculated the radial velocities of galaxies using their redshift, and postulated that if the cluster was in a mechanically stationary state, neither contracting nor expanding, then Newton's inverse square law of gravity was valid. The mass could then be calculated using the velocity distribution of its galaxies. In classical mechanics this is known as the virial theorem.

7

$$KE = \frac{-PE}{2} = \frac{-1}{2} \sum_i m_i \overline{v_i^2} \tag{1.14}$$

See Fig. 1 for a current plot of the velocity distribution of the Coma cluster.

The mass found using the virial theorem is compared to the expected mass when only the stars in the galaxies are taken into account. To do this the mass-to-light ratio, Y, is calculated. It is normalized such that the mass-to-light ratio of our sun is unity $Y_\odot = M_\odot / L_\odot = 1$. Our sun is not necessarily an exact representation of the mean in a large stellar population, so some deviation is expected. However, Zwicky calculated $Y_{coma} = 500$ [6]. Even after extensive analysis of the uncertainties involved, he maintained that his measurement was correct to within an order of magnitude. At that time, he did not postulate as to the nature of the unseen matter but simply stated that if the density measurement could be confirmed, then "we would get the surprising result that Dark Matter is present in much greater amounts then luminous matter." [1]

More recent studies of the Coma cluster have yielded a mass-to-light ratio of $Y = 182$, further confirming Zwicky's original order of magnitude claim [7]. Other surveys of virial masses have been conducted and in each galaxy cluster studied, large discrepancies have been seen between the luminous and virial masses. One study, using 89 clusters, yields a typical value of $Y = 250$ [8]. These results lead to a lower bound on the total matter density of $\Omega_m \approx 0.19$ [9].

1.2.2 Rotational Velocity of Spiral Galaxies

In 1939, the stars in the Andromeda galaxy (M31) were found to have approximately the same orbital velocity at all radii outside the central bulge [10]. This
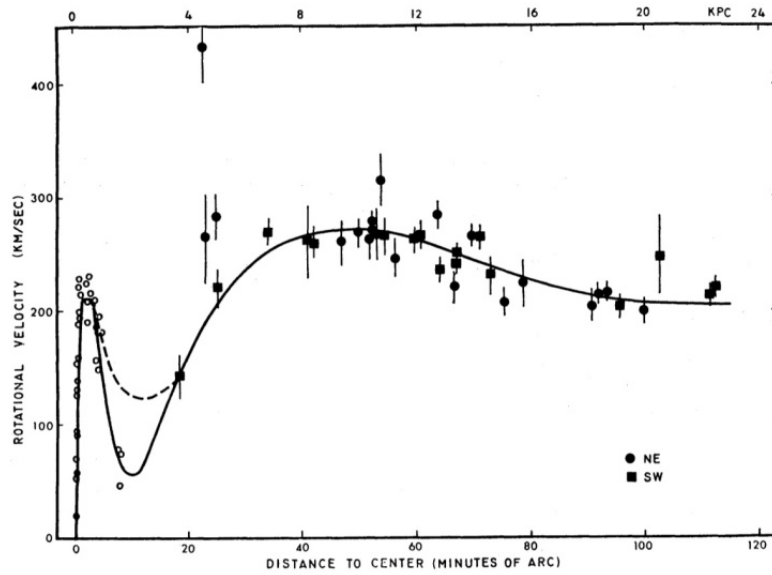
Fig. 2. Rotational velocities of stars in M31 as a function of distance from the center. (Fig. from [11])

was confirmed 30 years later by Rubin and Ford [11]. See Fig. 2 for a graph of the M31

rotational velocity curve. The rotational velocities of stars in spiral galaxies can be

calculated by measuring the Doppler redshift as a function of distance from the center. A

clearer picture can be obtained by using the 21cm atomic transition line of atomic

hydrogen (HI) due to HI extending further than the visible stars [12]. The luminous

matter is distributed like a falling exponential outside the central bulge.

$$I = I_0 e^{\frac{-r}{r_0}}$$
(1.15)

where I is the surface brightness and r the radius. If the mass distribution followed the

visible material the radial velocities would be once again given by Newtonian

mechanics. By equating Newton's 2nd law of motion and his law of gravitation, we get

an equation for the expected velocity of stars outside the central bulge.

9
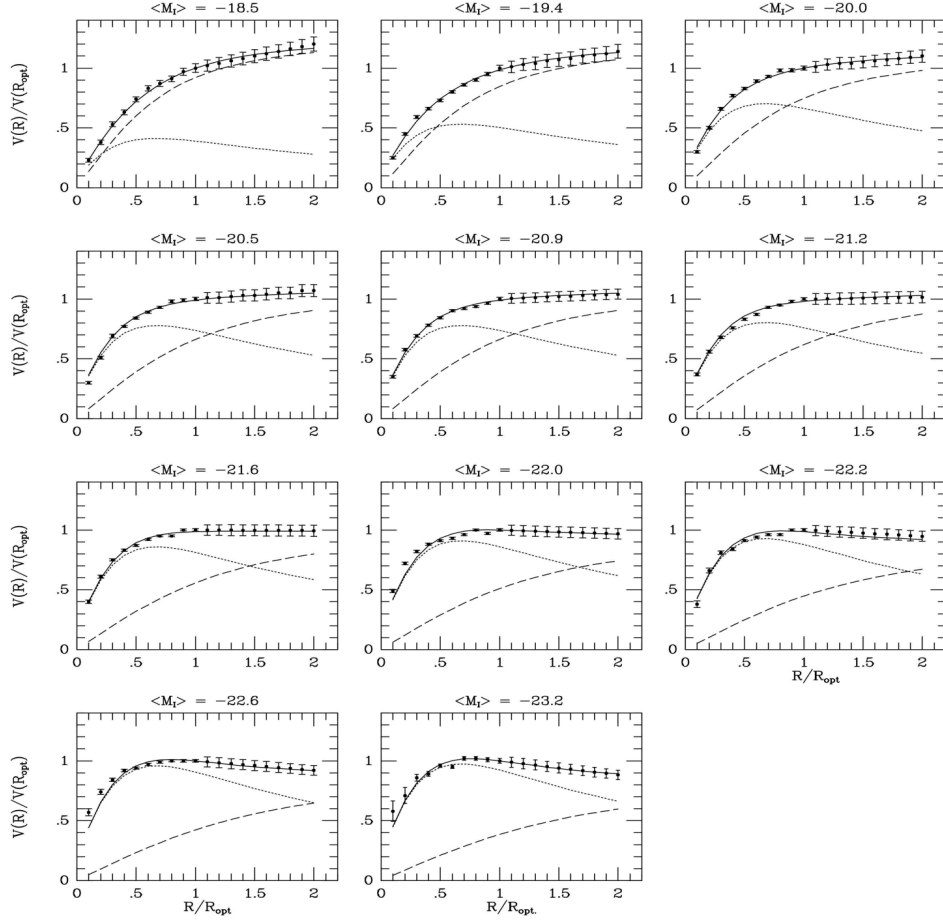
Fig. 3. The best two component fits to the universal rotation curve for spiral galaxies. Dotted line: Disk, Dashed line: Halo. (Fig. from [14])

$$v_{rot} = \sqrt{\frac{GM(r)}{r}} \qquad (1.16)$$

This implies that velocities at large distances would go as $v_{rot} \propto r^{-1/2}$. Instead they are found to be nearly constant. A constant velocity leads to a mass distribution of $M(r) \propto r$.

Other studies of spiral galaxies en mass (~1100) have shown, that they fit a universal rotation curve that is dependent on the luminosity [13][14]. As the luminosity decreases, the discrepancy increases between the mass calculated using the luminous

matter and the mass calculated using the rotation velocities. This picture of the spiral galaxy rotation curves shows that the mass of (gas + stellar disk) is insufficient to account for all the matter measured. The data requires the addition of an unseen halo of matter in which the galaxies embedded. This is where the isothermal Dark Matter halo model originates. Fig. 3 shows the rotation curves of several galaxies with the gas, stellar component, and halo included to fit the measured stellar velocities.

1.2.3 Gravitational Lensing

Gravitational lensing is the deflection of light from a distant object (lensing object) by the gravitational potential well of a massive object (lens object), a galaxy cluster for example, between the light source and the observer. This results in the light deviating from a straight line, instead following geodesics and reaches us from several points forming several warped images. This curvature of space-time is predicted by Einstein's theory of General Relativity and can be used to measure the mass between source and observer [15]. The effect is independent of the composition of the lens object. A more detailed discussion of gravitational lensing can be found in [16].

There are three types of gravitational lensing known as strong, weak, and micro. Strong lensing causes easily visible distortions with multiple images and arcs. It is caused by the deflection through larger angles that can result in very complicated images in the observer plane. It can be used as a tool for testing the distribution of mass in the lens, but it is not always possible to find a unique mapping onto the source plane. See Fig. 4 for an example of strong lensing.

Galaxy Cluster Abell 2218
Hubble Space Telescope • WFPC2
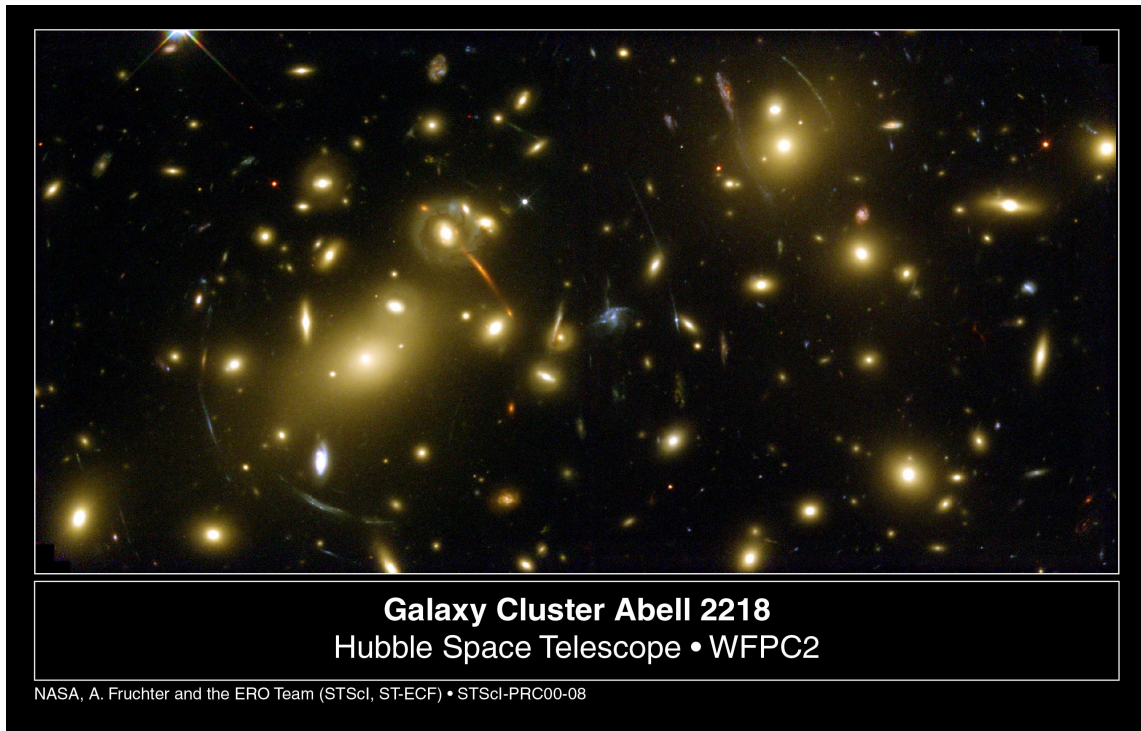
Fig. 4. Hubble Space Telescope image of the galaxy cluster Abell 2218. Strongly lensed galaxy images are clearly visible. (Fig. from [17])

Weak gravitational lensing is a much more subtle effect. The distortion of any one object is only ~1% elongation [18][19]. With weak lensing several individual sources around a lens object must be mapped to reconstruct the coherence of the distortion, or "shear". The shear measurements give the mass distribution of the lens.

Micro-lensing occurs when a smaller object passes between the observer and the source object, resulting in an amplification of the source luminosity. The lens causes the sources light to be focused, which causes an apparent increase in brightness. Experiments search for a change in luminosity of background object over time. Peaks in the data indicate the passage of a lens object in the foreground.
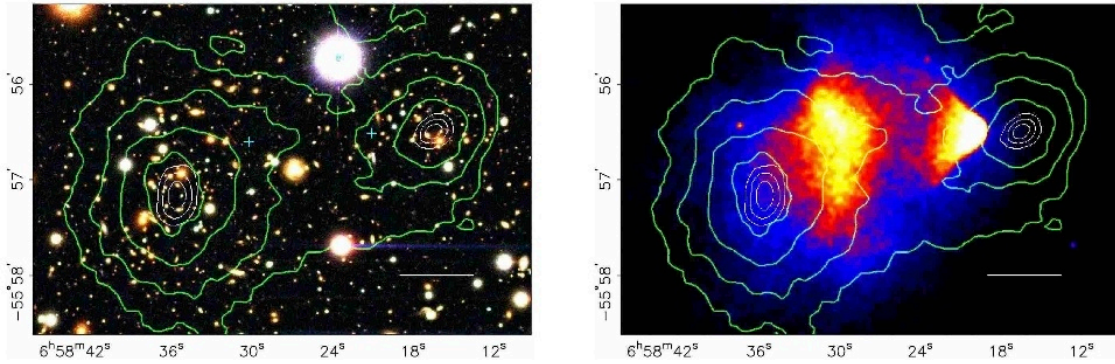
Fig. 5. The Bullet Cluster merger object showing the separation of the gas component from the Dark Matter component. The green contours indicate the mass distribution of the lens object, reconstructed using weak-gravitational lensing. The white contours are the peak of the mass distribution. Left: Optical image obtained with the Magellan Telescope. Right: X-ray image obtained by the Chandra X-Ray Observatory. (Fig. from [20])

By combining weak and strong lensing observations scientists have been able to reconstruct the mass density of galaxies and show that a dark component exists, which is in agreement with the observed virial masses. A study of 22 galaxies gives a mass-to-light ratio on average of 246^{+101}_{-87} $M_\odot/L_\odot$ [20].

One famous weak lensing observation is the Bullet Cluster merger object. The two main sources of mass for the clusters are non-interacting Dark Matter and hot X-ray emitting gas clouds [See Fig. 5]. The plasma is observed using X-ray emissions and the Dark Matter using lensing. If there were no Dark Matter component then the dominant mass would follow the gas but this is not observed. During a merger the two Dark Matter components pass right through each other interacting only gravitationally. Alternately, the gas clouds interact electromagnetically and are stripped away from their Dark Matter component. This results in the dominant mass being displaced from the observed baryonic
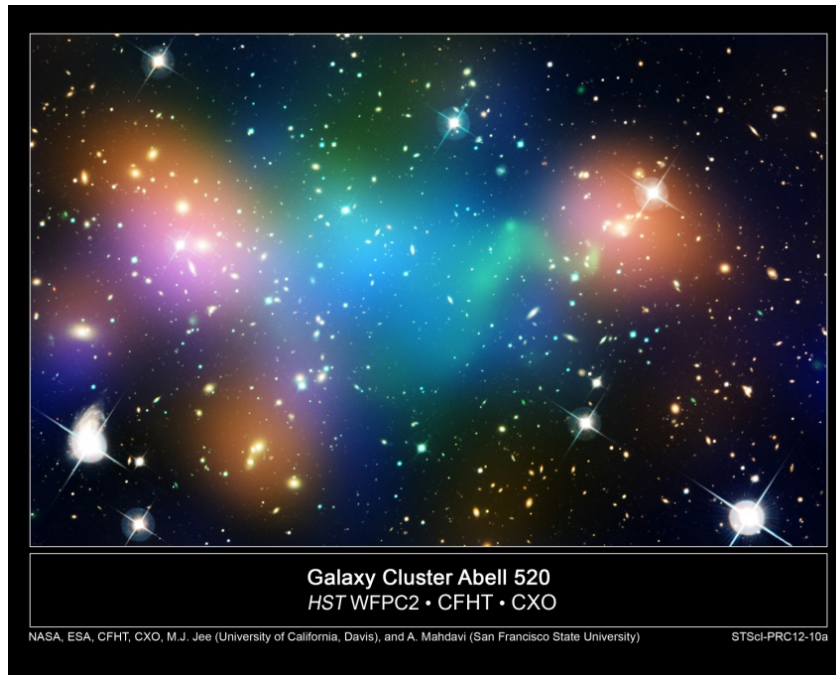
Fig. 6: Composite image showing the distribution of Dark Matter (blue), galaxies (gold), and hot gas (green). It is in the core of the merging galaxy cluster Abell 520, formed from a violent collision of massive galaxy clusters. (Fig. from [21])

matter. Further observations of other galaxy and cluster mergers yield similar separation of baryonic and Dark Matter components, suggesting a large non-luminous non-interacting matter component [See Fig. 6].

1.2.4 Type 1a Supernovae

In order to obtain relative fractions of Ω_m and Ω_Λ scientists need precise measurements of the acceleration rate of the expansion of the Universe. To obtain this, they measure the redshift as a function of distance for various galaxies and stars. In order to accurately measure distances, they employ objects of known luminosity or "standard candles". By observing how the luminosity of a standard candle changes with distance, they can accurately calculate the redshift of distant objects. Using this technique in the

nearby Universe gives values for the current rate of expansion, H_0, and for more distant objects it gives the expansion acceleration/deceleration of the Universe in the past. [22]

Type 1a supernovae are one type of standard candle used for these measurements. Type 1a are the explosions of white dwarf stars that are accreting mass from a binary companion star. White dwarfs are older stars that have lost their hydrogen envelope and have a mass less than the Chandrasekar (1.4 $M_\odot$) limit. The nucleus of these stars is typically oxygen and carbon, held up by electron degeneracy pressure. The thought is that these stars accrete mass from a binary companion star until they exceed the 1.4 $M_\odot$ mass threshold. At this mass, gravity overcomes the electron degeneracy pressure and the core collapses in a matter of seconds, releasing $\approx 10^{63}$ eV of energy (99% neutrinos [23]) in a supernovae explosion [22]. This situation is repeatable and has a characteristic light curve and peak luminosity. Thus making Type 1a SN an ideal choice for standard candle distance measurements.

For low redshifts (z < 0.2), objects which are nearby, the apparent brightness of objects, D_L, scales linearly with distance.

$$v = H_0 D_L \tag{1.17}$$

Usually it is reported as the distance modulus

$$\mu = 5\left(\log D_L - 1\right) \tag{1.18}$$

Eq. (1.17) gives a measurement of the current expansion rate of the Universe, H_0. For a recent compilation of Type 1a SN data, see Fig. 7. Earlier results have shown $H_0 = 71$ km/s/Mpc to 10% accuracy [22].

At larger redshifts (z = 0.3-1.0) the apparent brightness depends on the composition of Ω_m and Ω_Λ, (Ω_m = 0.3 and Ω_Λ = 0.7 for example). Using D_L measurements over high ranges, constraints can be placed on (Ω_m - Ω_Λ). Fig. 8 shows results from current Type 1a measurements as well as those from Baryonic Acoustic Oscillations (BAO) and the Cosmic Microwave Background (CMB) which will be discussed in the following sections. The combined allowed values are shown in grey.
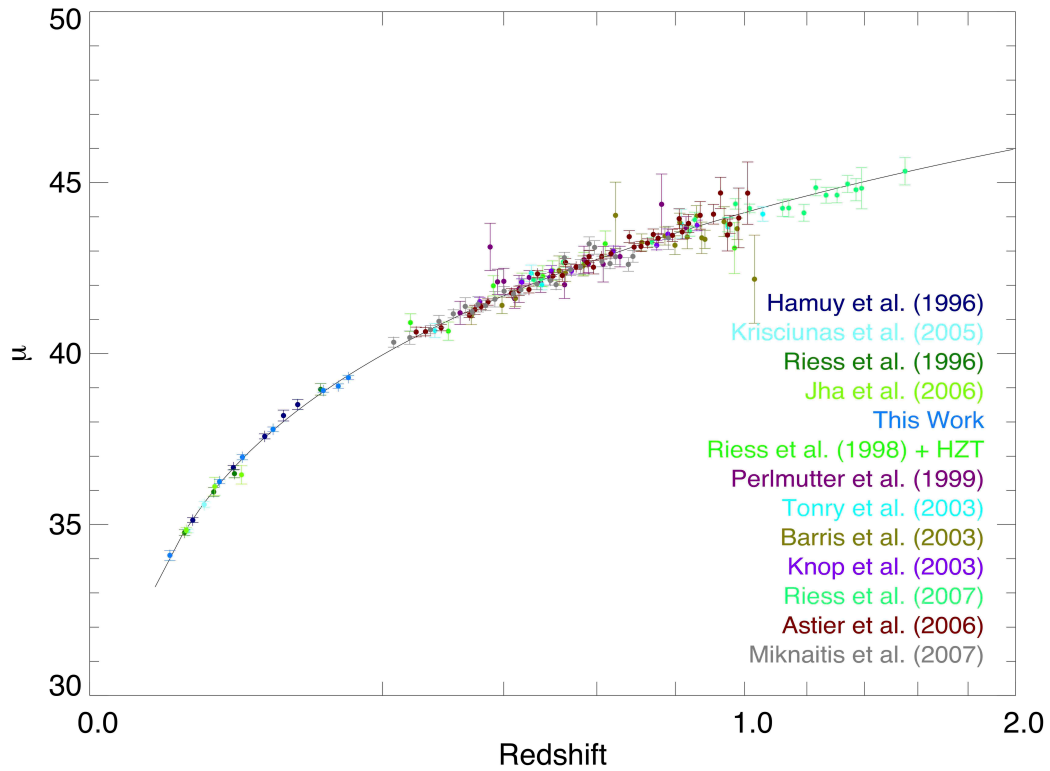
Fig. 7. Recent compilation of Type 1a supernovae distance modulus µ as a function of redshift. (Fig. from [24])

16
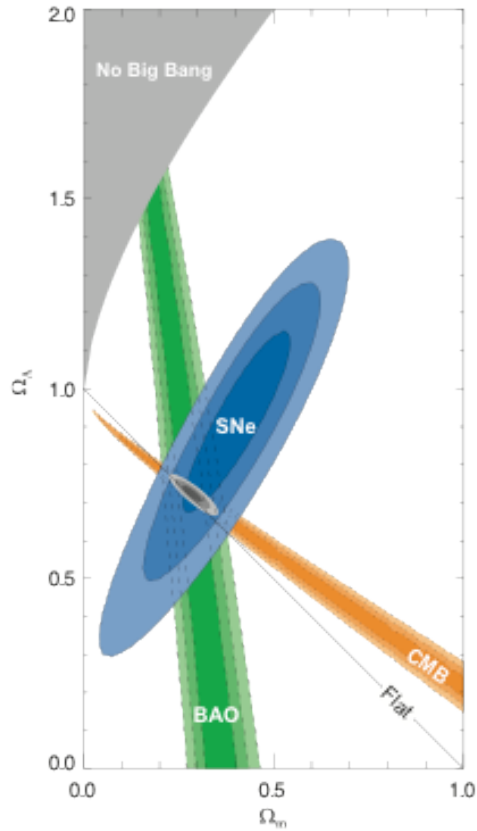
Fig. 8. Contours for 68.3%, 95.4%, and 99.7% CL for Ω_Λ and Ω_m. Data from the Union SN set (blue), CMB (orange), and BAO (green). (Fig. from [24])

1.2.5 Cosmic Microwave Background

The Cosmic Microwave Background (CMB) is an isotropic low energy radiation left over from the Big Bang that suffuses the entire Universe. Penzias and Wilson first detected it in 1964 [25] but scientists such as George Gamow, Ralph Alpher, and Robert Herman posited its existence and made approximate calculations of its intensity as early as the 1940's. They calculated the temperature of the primordial radiation to be $T_{CMB} \approx$ 5K. This corresponds to $\lambda = 2.9 \times 10^{-3}$ m which is in the microwave range, resulting in the

name Cosmic Microwave Background [15]. Current measurements place the average temperature at $T_{CMB} = 2.725K$ [26].

During the early Universe the temperature was greater then 3000K and all matter was a photon-baryon plasma coupled via Thompson scattering. As the Universe cooled, structures began to form under their own gravity. At around $t \approx 379,000$yrs the temperature cooled down to $T \approx 3000K$ and photons could no longer ionize atomic hydrogen as it formed. Consequently, protons and electrons combined to form neutral hydrogen and photons "decoupled" from baryons, scattering for the last time. This is known as the "time of decoupling" or "time of last scattering", t_{LS}. The Universe was no longer opaque to photons and those photons give us a snapshot of what the Universe looked like, since they are effectively frozen in the state they were in at t_{LS}. [15]

Prior to the time of last scattering, fluctuations created higher and lower density regions in the photon-baryon fluid. In the high-density regions, gravity attracted more mass, seeding the formation of structure. The outward pressure of radiation offset this gravitational pull. The two forces combined causing acoustic oscillations. When the photons scattered for the last time, the ones in high-density regions had slightly higher energy, and correspondingly higher temperatures. This left those regions of compression or rarefaction as hot and cold spots in the CMB. These fluctuations show up today as anisotropies in the CMB on the scale of μK. [27]

The CMB anisotropies were first measured to a resolution of $\theta > 7°$ by the Differential Microwave Radiometers (DMR) on the Cosmic Background Explorer (COBE) satellite in 1989 [28]. Several other experiments in the 1990's, BOOMERanG,

MAXIMA and DASI being examples, took data on the CMB [29]. One of the most precise measurements, $\theta \approx 0.2°$, has been taken by the Wilkinson Microwave Anisotropy Probe (WMAP) that was launched in 2001. WMAP has published updated measurements for over 9 years. The current map of the temperature fluctuations from WMAP are shown in Fig. 9 [4]. More recently, the Plank satellite launched in 2009 has made even more precise measurements of the CMB and its fluctuations [30].
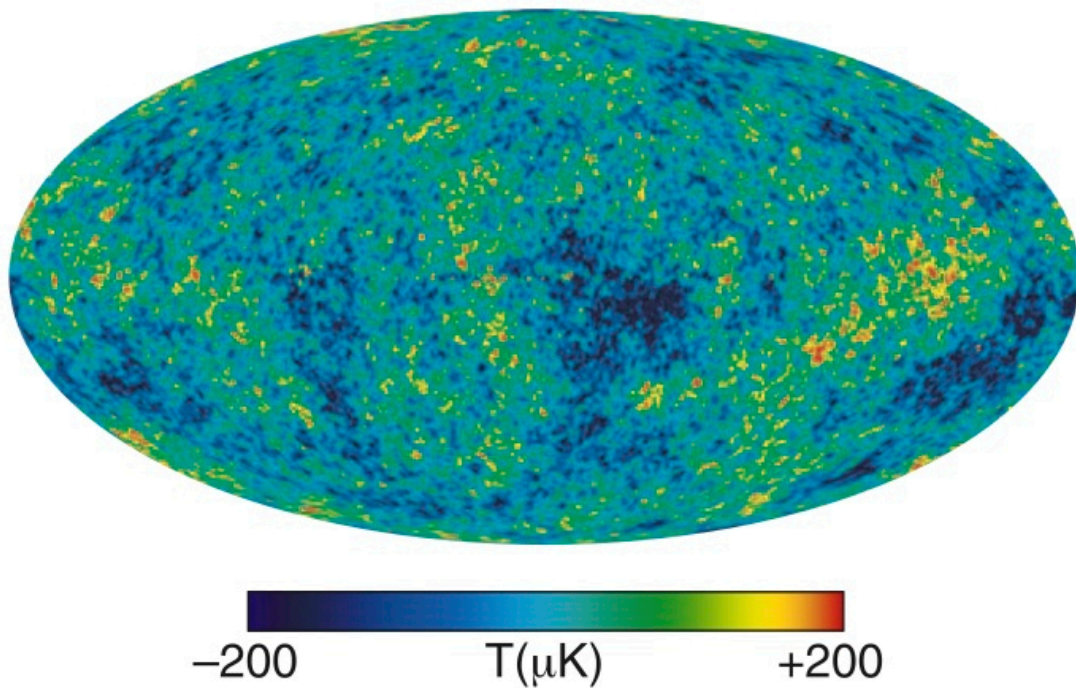
Fig. 9. Full sky map of the WMAP 9-year observations. (Fig. from [4])
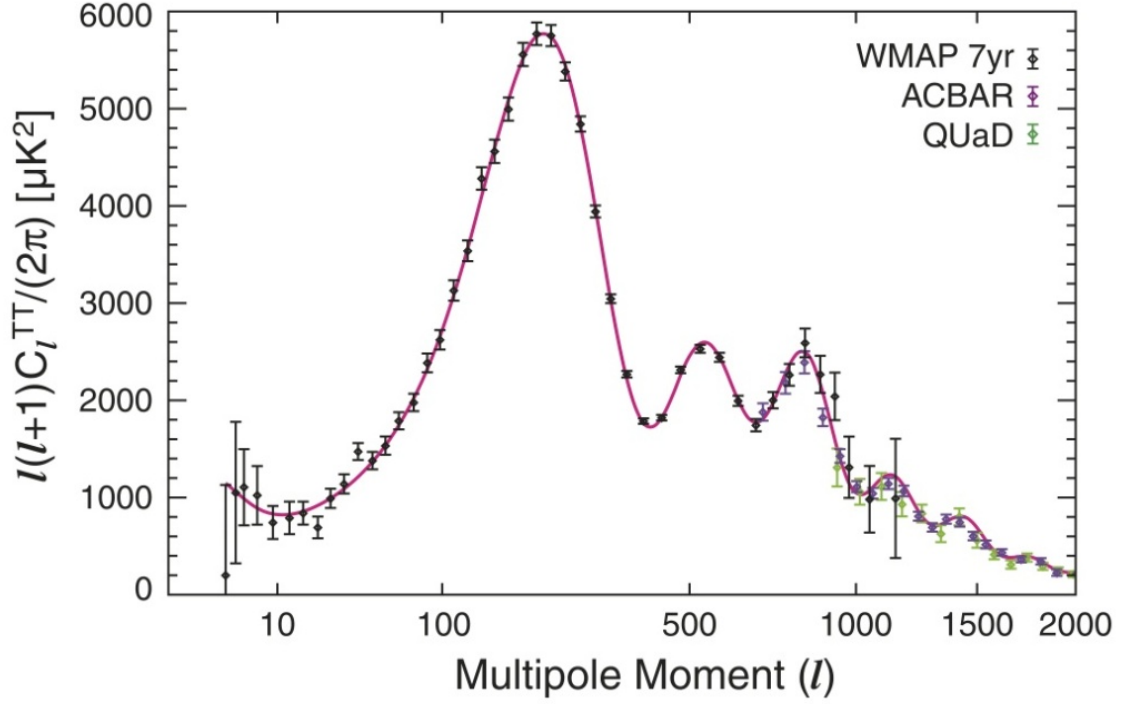
Fig. 10. The WMAP 7-year temperature power spectrum. The solid line shows the best fitting 6-parameter flat ΛCDM model to the WMAP data. Also shown is data from ACBAR [31] and QUaD [32] experiments. (Fig. from [28])

Several important cosmological parameters can be obtained from measurements of the CMB anisotropies [28]. In order to do this, the power spectrum must first be decomposed into a sum of spherical harmonics yielding the angular power spectrum. The angular power spectrum from the WMAP 7-year results is shown in Fig. 10. The deviations from the mean of the temperature in the $\hat{n}$ direction can be expressed as

$$\frac{\Delta T(\hat{n})}{T} = \sum_{l=0}^{\infty} \sum_{m=-1}^{+1} a_{lm} Y_{lm}(\theta, \phi) \tag{1.19}$$

An average for the angular power spectrum is given by

$$C_l = \left\langle \left| a_{lm} \right|^2 \right\rangle \tag{1.20}$$

20

and is observed in our sky as

$$C_l^{sky} = \frac{1}{2l+1}\sum_m |a_{lm}|^2 \tag{1.21}$$

For each multipole moment the temperature anisotropy, ΔT_1, is related to the angular

spectrum through the relationship

$$\Delta T_l = \sqrt{\frac{l(l+1)C_l^{sky}}{2\pi}} \tag{1.22}$$

The correlation function is the average covariance of the temperature fluctuations for all

points separated by an angle θ, and expressed in terms of Legendre polynomials gives

$$C(\theta) = \frac{1}{4\pi}\sum_l (2l+1)C_l P_l(\cos\theta) \tag{1.23}$$

The C_l coefficients are the multipole moments, usually expressed as a power spectrum of

the temperature fluctuations and are plotted as a function of l or θ.

$$\Delta_T^2 = \frac{l(l+1)C_l}{2\pi}\langle T \rangle^2 \tag{1.24}$$

The peaks in the spectrum are the acoustic oscillations from extreme

compression or expansion of the photon baryon fluid at t_{LS}. The first peak at $\theta \approx 1°$ and

$l \approx 200$ gives the angular size of the Hubble distance, the distance light can travel in the

age of the Universe, as seen from Earth. From the known acoustic size at a known

redshift the age of the Universe can be inferred as $t_0 = 13.75 \pm 0.12$ Gyr. [3]

The ratio of the heights of the first and second peaks gives a measurement of the

baryonic matter density at the time of recombination. This is because the amplitude of

the peaks is a measure of the gravitational compression, which is dependent on the

frequency of the oscillations, which in turn depend on the ratio of baryonic mass in the fluid [27]. The WMAP 9-year results measure $\Omega_b = 0.0463 \pm 0.0024$ [3].

The power spectrum can also estimate the total mass component of the Universe, Ω_m. After t_{LS} the CMB photons travel in and out of the gravitational potential wells. The well depth determines the degree to which they are red- or blue-shifted. If the potential changes between the time a photon falls into the well and the time it climbs out, the blue-shift will be different than the red-shift, causing a residual fluctuation in the temperature. This is known as the Sachs-Wolfe effect. The Integrated Sachs-Wolfe (ISW) effect is divided into two stages, early and late. The early ISW corresponds to a radiation-dominated to matter-dominated Universe and is the main source of anisotropies at scales larger the 10°. The total matter density is obtained from measuring the early ISW. The late ISW effect corresponds to the transition from matter-dominated to Λ-dominated Universe. Measurements of the late ISW place constraints on Ω_Λ. [33]

Accurate measurements of the CMB power spectrum give values for each of the density parameters as well as other cosmological quantities. By combining the WMAP and Plank results with other observations of large-scale structure, Baryonic Acoustic Oscillations (Section 1.2.6) and type 1a supernovae data (Section 1.2.4), we get the values listed in Table 1.

The total matter density, Ω_m, and the total baryon density, Ω_b, are two different values, measured independently from one another. This leads to the conclusion that the total mass in the Universe is actually about 6x that of the baryonic mass.

Table 1 The composition of the Universe. ΛCDM parameters from the combined data of WMAP 9-year results, BAO, and H_0 [3] and the Plank results with WMAP 9-year results [34].

The Composition of the Universe		
ΛCDM Parameters	WMAP + eCMB + BAO + H$_0$	Plank + WMAP
Ω_Λ	0.7135 ± 0.0096	0.685 ± 0.0018
Ω_m	0.2865 ± 0.0096	0.315 ± 0.018
Ω_d	0.2402 ± 0.0088	-
Ω_b	0.04628 ± 0.00093	-
H_0	69.32 ± 0.80	67.3 ± 1.2
t_0	13.772 ± 0.059	13.817 ± 0.048

The extra matter is thought to be non-baryonic Dark Matter.

$$\Omega_m = \Omega_b + \Omega_d \qquad (1.25)$$

1.2.6 Large Scale Structure and Baryonic Acoustic Oscillations

The fluctuations of matter density in the primordial photon-baryon fluid not only left their imprint on the CMB but also seeded the formation of large-scale structures, such as the galaxy clusters and super clusters that we observe today. Acoustic peaks occur because the density perturbations excite sound waves in the photon-baryon fluid. At the time of recombination, t_{rec}, around redshift z ~ 1000, the speed of sound in the fluid decreased and wave propagation ended. The baryon mass distribution is reflected in the maxima and minima of the anisotropy power spectrum. By observing what the distribution of baryonic matter was then, scientists today can construct a correlation

function, $\xi(\sigma,\pi)$, that measures the probability of finding a pair of galaxies with transverse separation, σ, and line-of-sight separation, π [35]. There should be a peak in the correlation function that corresponds to the length of the sound horizon, r_s. The sound horizon is the distance a sound wave could have traveled in the age of the Universe at t_{rec}. [36]

A slightly more simplified way to look at it is to start with an initial point perturbation, common to both baryons and Dark Matter, pre-recombination. As the Universe ages the Dark Matter perturbation grows in place, while the baryon component is carried outward in an expanding spherical wave. After recombination, the combined perturbations seed the formation of large-scale structure. The Dark Matter perturbation is dominant compared to the baryonic shell. The resulting acoustic feature that we can observe is a small single spike in the correlation function at r_s.

The Sloan Digital Sky Survey (SDSS) is a huge survey, covering over a quarter of the sky, that maps the local Universe in 3D. See Fig. 11 for an example of a typical red-shift map of the galaxies from SDSS.

The SDSS scientists analyzed a subset of over 46,000 Luminous Red Galaxies' (LRG) power spectrums in order to plot their correlation function. They found strong evidence (3.4σ) for an acoustic peak at $100h^{-1}$ Mpc scale, in good agreement with ΛCDM interpretations of the CMB data. (Fig. 12). [38]
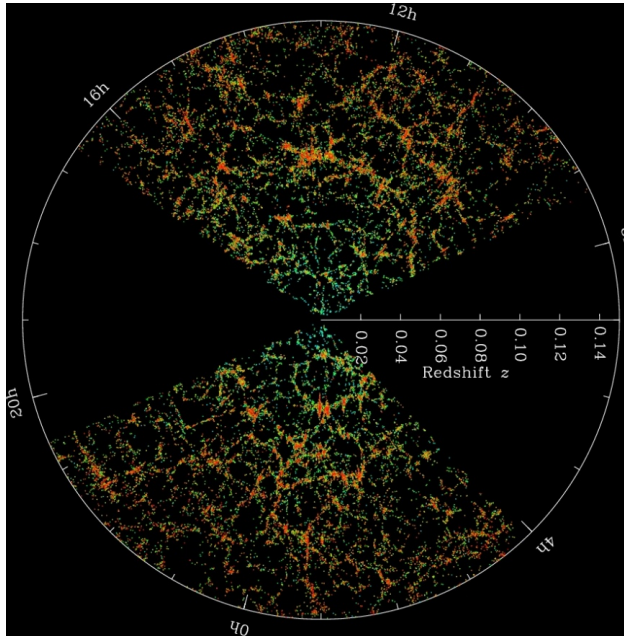
Fig. 11. SDSS 3-D map of the Universe. Galaxies are colored according to the age of their stars, more red being older stars. [Credit: M. Blanton and the Sloan Digital Sky Survey] (Fig. from [37])
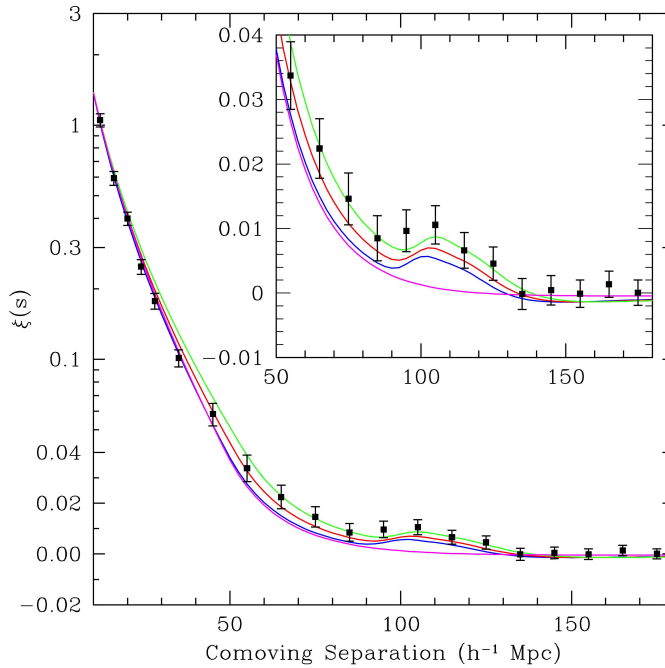
Fig. 12. The correlation function for galaxy separation from the SDSS LRG study. Different color lines correspond to different models of mass density parameters: $\Omega_b h^2 = 0.024$ and $\Omega_m h^2 = 0.12$ (green), 0.13 (red), 0.14 (blue). The magenta line corresponds to a pure CDM model and lacks an acoustic peak. The bump at $100h^{-1}$ Mpc has a significance of 3.4σ. (Fig. from [38])

This shows that there are indeed oscillations at $z \approx 1000$ and that they survive to be detected today at low redshifts. The small amplitude peak requires that matter that does not interact with the proton-baryon fluid, i.e. Dark Matter, exists at $z \sim 1000$. The detection of the low redshift oscillations is a confirmation of the ΛCDM theory for structure formation in the Universe, since the narrowness of the peak would be difficult to attain with alternate models of cosmological growth. A fully baryonic model would produce a larger amplitude peak then observed. Hot Dark Matter wouldn't have started galaxy formation soon enough and would have resulted in larger structures then we observe. [39]

The Baryonic Acoustic Oscillation data (BAO) sets constraints on the total baryonic matter density in the Universe because the observed amplitude of the oscillation is incompatible with a high baryon fraction. Fig. 13 shows a map of the allowed phase space Ω_m vs Ω_b. Combining BAO with WMAP data further constrains the allowed matter density fraction. [24]

1.2.7 Big-Bang Nucleosynthesis

Big-Bang Nucleosynthesis (BBN), first proposed by Alpher, Bethe and Gamow in 1948 [40], describes a brief epoch in which nuclear fusion created the light elements like D, ^{3}He, ^{4}He, ^{6}Li and ^{7}Li that we observe today. Heavy elements are created in star cores and supernovae but the lighter elements formed in great abundance for only a few minutes near the beginning of the big bang. The relic abundances of these elements today give us valuable insight into the contents and conditions of the Universe in its first few minutes. [41]
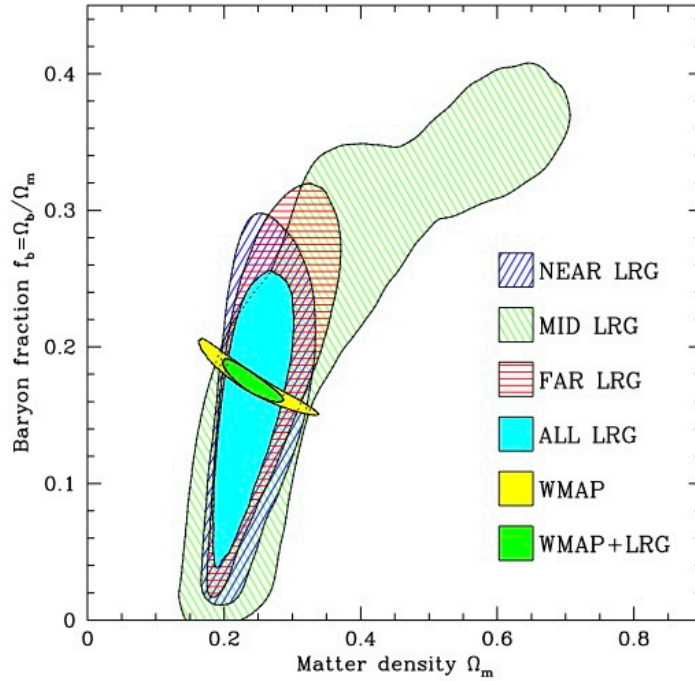
Fig. 13. Constraints on the total matter density (Ω_m) and the baryonic matter ratio (Ω_b/Ω_m) from the SDSS LRG study. The figure includes data from LRG, and WMAP CMB measurements, as well as the combination of both data sets. (Fig. from [36])

Current BBN theory presents a timeline as follows. (See [42] or [43] for a more comprehensive discussion) Initially, at t < 0.1s after the big bang, the Universe was hot and dense enough to maintain equilibrium levels of most particles (neutrinos, $e^{\pm}$ pairs, photons, and nucleons). The charged-current weak interactions were able to maintain the neutron/proton ratio at its equilibrium value of

$$\left(\frac{n}{p}\right)_{eq} = e^{\frac{-\Delta m}{T}}$$

(1.26)

The Universe continued to cool and expand, which caused the lighter protons to be favored over their heavier companion neutrons, decreasing the ratio to around ~1/6. When the Universe reached t ~ 1sec the weak interactions were too slow to maintain

equilibrium and the n/p fell to ~1/7, moving further from equilibrium. The ratio depends on the weak interaction rates and the early Universe expansion rates, as well as possible neutrino asymmetry. Any deviation from the standard model will show up in the relative numbers of neutrons and protons in complex molecules.

Meanwhile the protons and neutrons are interacting to form deuterium $p + n \rightarrow D + \gamma$. The gamma background is still at a high enough energy, $E_\gamma \sim 3T_\gamma \geq$ few MeV, to photo-disassociate any deuterium before more complex nuclei can form. This situation persists until the temperature drops below the binding energy so that there aren't sufficient γ's around to destroy the deuterium before it can capture any additional nucleons. This takes place at about t ~ 2000s (T ~ 80K). At this point the $e^\pm$ annihilations have ceased and the BBN begins in earnest. ^{4}He is the most tightly bound of the formed nucleotides. There are no stable nuclei with mass A = 5, so all the available neutrons are made into ^{4}He. The relic abundance of ^{4}He is limited by the neutron availability at that time.

Coulomb suppressed reactions of ^{4}He with D, ^{3}H or ^{3}He are the only way for nuclear processes to move past the mass 5 gap for stable nuclei. Therefore, the abundance of heavier nucleotides is depressed well below that of the lighter masses. Those that do occur in cosmologically interesting amounts are mainly ^{7}Li and ^{7}Be, the later of which is unstable and decays to ^{7}Li. There is another gap at A = 8 which limits the BBN to producing nucleotides up to mass A = 7 in any measureable quantities.

When the Universe reaches $T \leq 30 keV$ at around t ~ 20min, the neutrons have all been incorporated into ^{4}He. Coulomb barriers suppress all the rest of the nuclear

reactions. BBN ends and no relic nuclides are created or destroyed until the first stars form.

The amounts of primordial nuclei all depend on one parameter, the ratio of baryons to photons

$$\eta = \left(\frac{n_b}{n_\gamma} \right) \tag{1.27}$$

As the Universe expands the densities all decrease. According to the standard model, after $e^{\pm}$ annihilation, the numbers of baryons and CMB photons in a commoving volume stay the same. This means that η measured now, at recombination, and at BBN should all be equal.

The evolution of each of the post BBN nuclides is different, as are the astronomical objects they are observed in and the observation techniques used. So the systematic errors in each observation are uncorrelated. For example, deuterium is measured from the absorption lines in high redshift quasars [44] and ^{4}He abundance can be inferred from HII regions in dwarf galaxies [45]. Both parameters are in good agreement with the CMB and SDSS for the baryonic density parameter [3][45]. The combined results of various experiments to observe BBN relic abundances are shown in Fig. 14. The ^{7}Li abundance, measured in poor metal stars (Population II), is a factor of 2-3x too small [48]. This could be due to systematic errors not accounted for or to new physics. Despite this all the primordial abundances point to a baryonic matter density much smaller then the total mass density of the Universe. Lending further support to

Dark Matter. Upcoming experiments and observations will hopefully clarify the ^{7}Li

problem and offer new solutions.
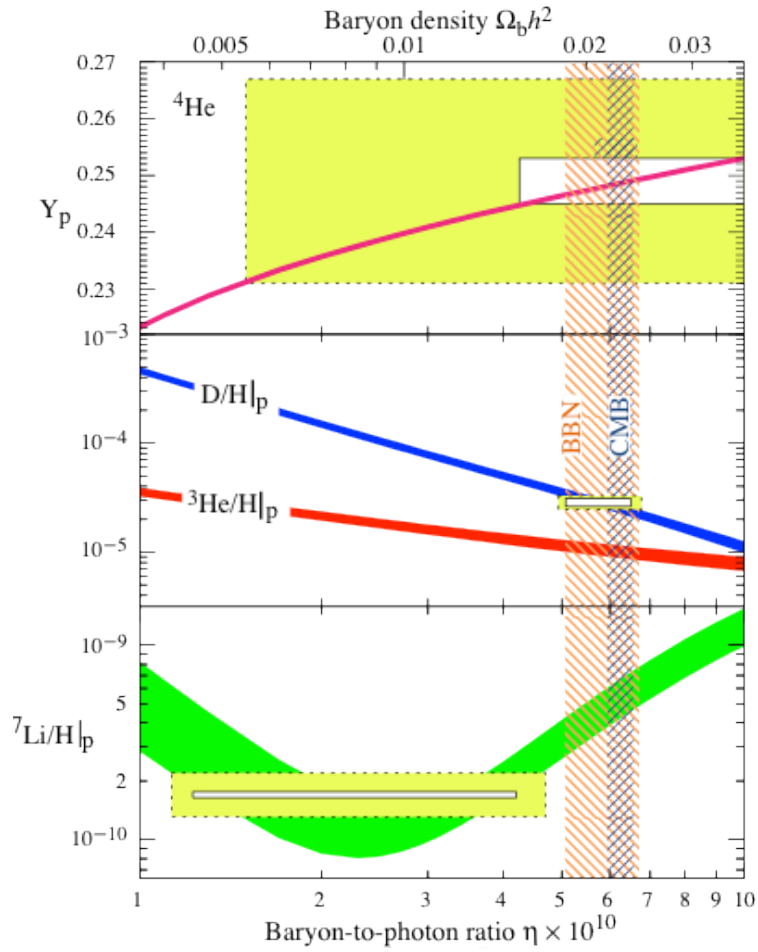
Fig. 14. BBN standard model predicted abundances of ^{4}He, D, ^{3}He, and ^{7}Li. The bands show 95% CL ranges. Smaller boxes: $\pm2\sigma$ stat. errors; Larger boxes: $\pm2\sigma$ stat. and sys. errors. Narrow band: CMB measurement of the cosmic baryon density 95% CL; Wider band: BBN range 95% CL. (Fig. from [43])
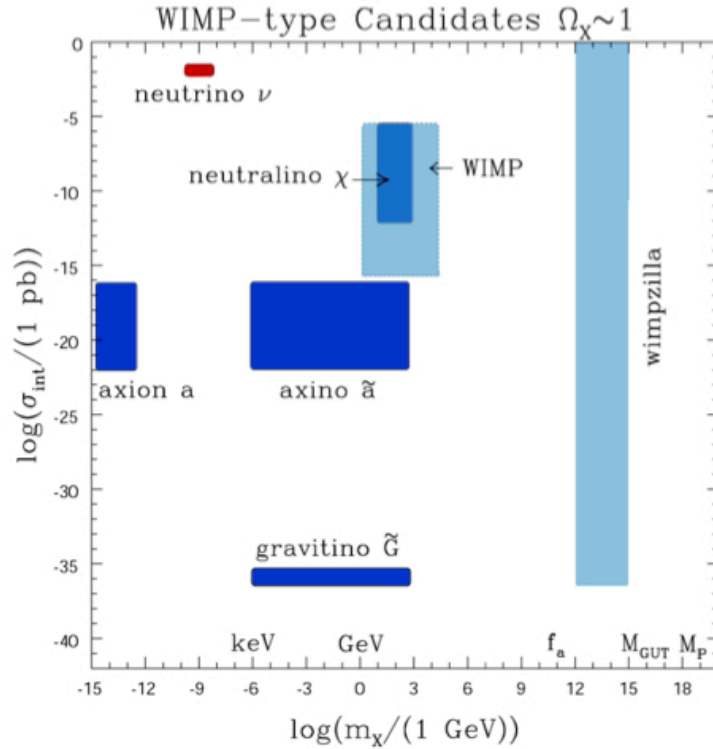
Fig. 15. Some well-motivated WIMP-type particles. σ_{int} represents a typical order of magnitude of interaction strength with ordinary matter. The neutrino is hot DM, which is disfavored. The "WIMP" box represents several possible candidates. (Fig. from [47])

1.3 Dark Matter Candidates

The previously discussed observations and theories point us to what Dark Matter needs to be, despite most of the evidence telling us what is isn't. We know that it must be weakly interacting, i.e. cannot interact via the electromagnetic force, so it is dark. It must have the correct relic density to describe the structure formation as we see it. Also, it must be stable on the time scale of the Universe so that it is still around to detect. Possible Dark Matter particles include axions, sterile neutrinos, weakly interacting massive particles and a plethora of other possibilities. (See Fig. 15) Only neutrinos, WIMPs and axions will be discussed further here. [43]

31

1.3.1 Neutrinos

If we start with the standard model then only the neutrino fits the aforementioned requirements. It is worth taking a look at it as a possible candidate for Dark Matter. We know that the neutrino played a role in the formation of light nuclei (Section 1.2.7) but the combined observations of the CMB anisotropies and SDSS have set an upper limit on light neutrino mass of $\Omega_v h^2 \leq 0.0062$ at 95% C.L. [43] If there were large amounts of primordial neutrinos they would have caused a damping in the oscillations of the photon-baryon fluid. We would see stronger CMB anisotropy peaks than we currently observe. Also, they would have affected the expansion rate of the Universe, shifting the position of the acoustic peaks. By far the most telling argument against neutrinos is that they are relativistic at decoupling, hence "Hot" Dark Matter. Hot primordial neutrinos would have smoothed out fluctuations at small scales (≤ 40 Mpc). If that was the case then the Universe would have formed in a "top-down" structure [48]. In other words, the large structures formed first, then the smaller ones later. Observations put the Milky Way being older than the local group [49], which makes this scenario unlikely. While neutrinos do contribute a non-zero component to Dark Matter, the majority of the mass must be a non-relativistic, "cold" particle.

1.3.2 Axions

Another well-motivated candidate for cold Dark Matter is the axion. They were first postulated in 1977 to solve the strong CP-violation problem in quantum chromodynamics [50]. As discussed in [51] axions are pseudo-Nambu-Goldstone bosons associated with the spontaneous breaking of Pecci-Quinn (PQ) U(1) symmetry.

32

Although they are very light particles (~µeV) axions still constitute cold Dark Matter because they are produced non-thermally [52]. Even at this low mass they should represent a cosmologically interesting relic density and many experiments are endeavoring to detect them, so far with negative results [53]. The Axion Dark Matter Experiment (ADMX)[52], CERN Axion Solar Telescope (CAST)[54] and PVLAS [55][56] are just a few of the experiments involved in axion searches. See [43] for further details on the cosmology and experiments connected to the axion.

1.3.3 WIMPs

Today the most favored of the many Dark Matter candidates is the Weakly Interacting Massive Particle (WIMP). WIMPs have a theoretical mass range of ~1 GeV to a few TeV, and an interaction cross section on the order of the weak scale. If such a particle does exist, then theoretically it could have a measureable relic abundance today that can be calculated in a straight forward manner [57]. The general argument goes as follows: Start with a new stable particle, call it χ. Just after the Big Bang, the Universe was hot and dense, χ exists in thermal equilibrium as long as the temperature exceeds its mass, m_χ. This equilibrium is maintained by the creation and annihilation with its antiparticle and the lighter particles (such as quarks and leptons), $\chi\bar{\chi} \rightarrow l\bar{l}$ or $l\bar{l} \rightarrow \chi\bar{\chi}$. In thermal equilibrium the number density of χ is

$$n_\chi^{eq} = \frac{g}{(2\pi)^3} \int f(\vec{p}) d^3\vec{p} \qquad (1.28)$$

where g is the number of internal degrees of freedom for χ and $f(\vec{p})$ is the Fermi-Dirac or Bose-Einstein distribution. As long as the temperature remains above the mass of the

particle then $n_\chi^{eq} \propto T^3$ so there are roughly as many particles as there are photons. Once the temperature is below m_χ then the number density is Boltzmann suppressed and follows

$$n_\chi^{eq} \approx g\left(\frac{m_\chi T}{2\pi}\right)e^{\frac{-m_\chi c^2}{k_B T}}$$ (1.29)

If the expansion of the Universe were slow enough that χ could maintain thermal equilibrium, then the number density today would be exponentially suppressed into non-existence. Fortunately for us that is not what takes place. As the temperature drops, the number density drops exponentially and the rate of annihilation, Γ_A, also decreased.

$$\Gamma_A = n_\chi \langle \sigma_A v \rangle$$ (1.30)

where σ_A is the annihilation cross section and v is the relative velocity of the two particles. When Γ_A becomes less than the expansion rate of the Universe ($\Gamma_A < H$) the annihilation process stops or "freezes out", χ falls out of equilibrium and the relic abundance from that time remains today. See Fig. 16 for an illustration of that process.

Assuming typical weak scale numbers, the freeze out temperature can be approximated [57] at

$$T_f \approx \frac{m_\chi}{20}$$ (1.31)
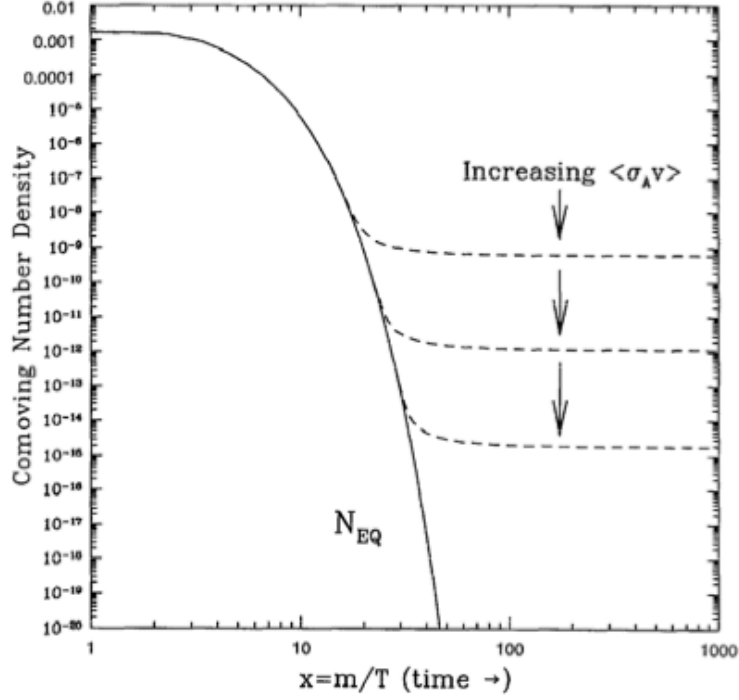
Fig. 16. The commoving number density of a WIMP in the early Universe. Dashed Curves: Actual abundance. Solid Curve: Equilibrium abundance. (Fig. from [57])

which results in the approximate mass density today of

$$\Omega_\chi h^2 = \frac{m_\chi n_\chi}{\rho_c} \approx \frac{\left(3x10^{-27} cm^3 / s\right)}{\langle \sigma_A v \rangle} \tag{1.32}$$

Eq. (1.31) turns out to be independent of the WIMP mass except for logarithmic corrections. The natural mass scale for this particle, assuming a weak interaction cross section $\langle \sigma_A v \rangle = 10^{-36} cm^3 / s$, is about a GeV. The result is $\Omega_\chi h^2 \approx 0.1$, assuming $h \approx 0.7$, gives an estimated value for non-baryonic matter close to what was discussed in Section 1.2.5. [51][57]

1.3.4 "So what is it exactly?"

Assuming that the WIMP is the correct choice for CDM, we are still faced with the question of "What is it exactly?" The term WIMP is still a generic name for a host of possible particles that show up in many theories. Most of them come out of the theory of supersymmetry (SUSY). A detailed explanation of supersymetry is beyond the scope of this thesis and can be found for example in [43] and [57]. Supersymmetry introduces a plethora of new particles, one superparticle for each standard model particle. They differ by a half-unit of spin so each fermion gets a supersymmetric boson and vice-versa. For example, the electron (fermion) has a selectron (boson) superpartner, and the photon (boson) has a photino (fermion) superpartner. If SUSY was a perfect symmetry then the masses for these new particles would be the same as their partners, but experiments have shown no evidence for this. It is postulated that SUSY is a broken symmetry and the masses of the superpartners must be greater than their standard model counterparts and have yet to be observed. In order to make predictions using SUSY, scientists have to first make a number of assumptions/constraints to narrow down the 100 or so free parameters into something a bit more tractable. This results in many different SUSY theories that span a large parameter space. What is useful is that in nearly all of them, there is a suitable DM candidate particle. The WIMP candidate from these theories is typically the Lightest Supersymmetric Particle (LSP). The LSP is a stable particle if R-parity is conserved. This is the symmetry that makes the proton stable, so it is not an unreasonable assumption. Of the many possible sub-theories of SUSY the most

compelling is the Minimal Supersymmetric Model (MSSM), which has the neutralino as a possible LSP. This theory predicts one superpartner for each standard model particle and two Higgs bosons. The exact composition of the neutralino is still unknown. It is usually presented as a superposition of the superpartners for the photon, Z-boson, and Higgs boson (photino, zino, and higgsino). Even if this is not the case other possibilities for a WIMP candidate will have a similar density parameter, and will be sufficient to solve the CDM problem. [43][51][57]

2. DIRECT DETECTION

The focus of this section is to describe the direct detection of Dark Matter. This is the interaction of WIMPs with Earth based detectors. First, the general model of the Universe is presented, followed by a short review of the basic physics of direct detection experiments. Then a few of the experimental efforts and the results in the search for low-mass WIMPs are discussed.

2.1 The Halo Model

The general agreement is that our galaxy is embedded in a large spherically symmetric halo of Dark Matter. It's important to understand the density and velocity distribution of the WIMPs. These are calculated using measurements of the rotation curves for the Milky Way. Most measurements agree that the local density is in the range of 0.2 - 0.8 GeV/cm^3 with the preferred value typically at $\rho_0 = 0.4 \, GeV\big/_{c^2 cm^3}$ [48]. The Dark Matter acts like an ideal gas with a Maxwellian velocity distribution.

$$f\left(\vec{v}, \vec{v}_E\right) = e^{-\left(\vec{v} - \vec{v}_E\right)^2 \big/ v_0} \qquad (2.1)$$

where $\vec{v}$ is the velocity of the DM particle onto the target nucleus,

$v_0 = \bar{v} = \left\langle v^2 \right\rangle^{\frac{1}{2}} \approx 220 \, km\big/_s$ is the average (most likely) velocity [58]. $\vec{v}_E$ is the Earth's velocity relative to the DM halo given by the sum of the galactic rotation speed, the rotation of the Sun relative to nearby stars, and rotation of the Earth relative to the Sun. $\vec{v}_E$ varies as the Earth orbits the Sun and is approximately

$$v_E \approx 244 + 15\sin(2\pi y)\frac{km}{s} \tag{2.2}$$

where y is the fraction of the year elapsed since March 2nd. This variation shows up in detectors as an annual modulation rate in the DM signal on the order of 3% [59]. The maximum velocity of DM is equal to the galactic escape velocity since any particle with a greater velocity would escape. Its value has been measured by RAVE survey to lie within $498\,\frac{km}{s} < v_{esc} < 608\,\frac{km}{s}$ at 90% C.L. The median likelihood is reported at

$v_{esc} = 544\,\frac{km}{s}$ [58].

2.2 WIMP Signals

WIMPs interact via direct scattering off a nucleus of ordinary matter. Although WIMP-nucleon interactions are expected to have a very small interaction cross sections, on the order of 10^{-41}cm^2. As small as this rate is, detection is still possible in an experiment with a large enough mass and low enough background. In this section we calculate the rate of these interactions and their expected energy range in order to get an idea of what the signal should look like in these types of detectors. It follows a more complete review given by Lewin and Smith in [59].

The differential event rate observed for nuclear recoils is in general featureless and smoothly decreasing with decreasing energy. In its simplest form should look like

$$\frac{dR}{dE_R} = \frac{R_0}{E_0 r} e^{-E_R/E_0 r} \tag{2.3}$$

where E_R is the recoil energy, E_0 is the most likely kinetic energy of the incident WIMP

with mass M_χ, the target nucleus mass is M_T, and the kinematic factor r is

$$r = \frac{4M_\chi M_T}{\left(M_\chi + M_T\right)^2} \qquad (2.4)$$

R is the event rate per unit mass and R_0 is the total event rate. The recoil energy of a

target nucleus hit by an incident WIMP of energy $E = \frac{1}{2}M_\chi v^2$ at an angle θ is

$$E_R = rE\frac{\left(1 - \cos\theta\right)}{2} \qquad (2.5)$$

  The actual signal observed is of course much more complicated than Eq. (2.3).

To break down into slightly more manageable pieces, we can rewrite it as

$$\left.\frac{dR}{dE_R}\right|_{obs} = R_0 S(E)F^2(E)I \qquad (2.6)$$

where S(E) is called the modified spectral function. It takes into account the relative

motion of the detector system, including annual modulation, the efficiency of nuclear

recoils compared to electron recoils, the elemental composition of the target, and the

limits based on the instrumentation of the detector. $F^2(E)$ is the form factor correction

due to the finite size of the nucleus. It has a value <1 and is dependent on the nuclear

radius and recoil energy. I is the interaction function which takes into account the

differences between spin-dependent and spin-independent nuclear interacts. R_0 is the

unmodified rate for a stationary earth and can be estimated from the observed

differential spectrum.

2.2.1 Total and Differential Event Rates

Before adding in the form factor correction (Section 2.2.2) and the interaction spin-component (Section 2.2.3) it is important to cover the equations describing the basic event rates for elastic nuclear recoil of WIMPs off a target nucleus. Not all of them are necessary to get an idea of what is being represented and only a part of the full derivation from [59] is presented here.

The differential particle density of WIMPs can be expressed as

$$dn = \frac{n_0}{k} f\left(\vec{v}, \vec{v}_E\right) d^3\vec{v} \tag{2.7}$$

k is the normalization constant such that n_0 is the mean DM particle density

$$\int_0^{v_{esc}} dn = n_0 \tag{2.8}$$

When the velocity of the WIMP onto the target is allowed to be $0 \le \vec{v} < \infty$ then

$$k = k_0 = \left(\pi v_0^2\right)^{\frac{3}{2}} \tag{2.9}$$

and with a more accurate, truncated velocity $\left|\vec{v} + \vec{v}_E\right| = \vec{v}_{esc}$ then

$$k = k_1 = k_0 \left[erf\left(\frac{v_{esc}}{v_0}\right) - \frac{2}{\sqrt{\pi}} \frac{v_{esc}}{v_0} e^{\frac{-v_{esc}^2}{v_0^2}} \right] \tag{2.10}$$

The event rate per unit mass on a target is

$$dR = \frac{N_0}{A} v\sigma \cdot dn \tag{2.11}$$

where N_0 is Avogadro's number, σ is the cross section per nucleon and A is the atomic mass of the target in AMU. For now assume no form factor corrections, these are added

41

in Section 2.2.2. The interaction cross section is set to a constant, $\sigma = \sigma_0$. R_0 is defined as the event rate assuming a stationary Earth, $v_E = 0$, and infinite escape velocity.

$$R_0 = \frac{2}{\sqrt{\pi}} \frac{N_0}{A} n_0 \sigma_0 v_0 \tag{2.12}$$

The total rate is then

$$R = R_0 \left(\frac{k_0}{k}\right) \frac{1}{2\pi v_0^4} \int v f\left(\vec{v}, \vec{v}_E\right) d^3\vec{v} \tag{2.13}$$

where $f(\vec{v}, \vec{v}_E)$ is from Eq. (2.1). The differential form is

$$dR = R_0 \left(\frac{k_0}{k}\right) \frac{1}{2\pi v_0^4} \left[v f\left(\vec{v}, \vec{v}_E\right) d^3\vec{v} \right] \tag{2.14}$$

We are primarily interested in the recoil rate inside some finite energy range. To calculate those ranges refer back to Eq. (2.5) for E_R. Assume that the scattering is isotropic in $\cos(\theta)$ and the recoils will then be evenly distributed between 0 and rE. The minimum energy, $E_{min} = E_R / r$, is the smallest WIMP energy that can give a recoil energy of E_R. Using $E_0 = \frac{1}{2} M_\chi v_0^2 = \left(\frac{v_0}{v}\right)^2 E$, $v_{min} = v_0 \sqrt{\frac{E_R}{rE_0}}$ and Eq. (2.14) the differential event rate becomes

$$\frac{dR}{dR_E} = \frac{R_0}{rE_0} \left(\frac{k_0}{k}\right) \frac{1}{2\pi v_0^2} \int_{v_{min}}^{v_{max}} \frac{1}{v} f\left(\vec{v}, \vec{v}_E\right) d^3\vec{v} \tag{2.15}$$

We are of course interested in this value with a non-zero v_E and finite v_{esc}

$$\frac{dR(v_E, v_{esc})}{dR_E} = \frac{k_0}{k_1} \left[\frac{dR(v_E, \infty)}{dE_R} - \frac{R_0}{rE_0} e^{\frac{-v_{esc}^2}{v_0^2}} \right] \tag{2.16}$$

42

$$\frac{dR(v_E, \infty)}{dR_E} = \frac{\sqrt{\pi}}{4} \frac{R_0}{rE_0} \frac{v_0}{v_E} \left[erf\left(\frac{v_{min} + v_E}{v_0}\right) - erf\left(\frac{v_{min} - v_E}{v_0}\right) \right] \qquad (3.17)$$

In order to get accurate values for the expected event rates, we still need to take into

account non-zero momentum transfer and the spin component of the target nucleus.

2.2.2 Nuclear Form Factor

The nuclear form factor is important when the momentum transfer to the target

nucleus is taken into account

$$q = \sqrt{2M_T E_R} \qquad (2.18)$$

As long as the nucleus is small compared to the de Broglie wavelength $\lambda = h/q$ (where

$h = 2\pi\hbar$) then it can be treated as a point particle. In this case the form factor is set $F = 1$

and there are no corrections to the effective cross section. For small q the cross section

can be assumed constant, $\sigma = \sigma_0$, for $q \rightarrow 0$ with respect to recoil energy. At some

finite recoil energy the de Broglie wavelength is no longer small compared to the

effective nuclear radius and the form factor becomes a relevant correction to the cross

section,

$$\sigma = \sigma_0 F^2(q) \qquad (2.19)$$

The effective cross section decreases with increasing recoil energy. The physical

interpretation of F(q) is a loss of coherence in the scattering amplitudes per nucleon for

$q > 0$ such that they do not add in phase which correspondingly suppresses the cross

section.

Scattering comes in two forms, spin-independent (SI) and spin-dependent (SD).

For SI the WIMP can scatter off any nucleon but for SD it can only scatter off an

unpaired nucleon. To approximate the form factor we start with the plane wave, or first

Born approximation. Then it is just the Fourier transform of the nucleons possible

scattering centers, ρ(r), is the target nucleus. Assuming a spherically symmetric

distribution the form factor looks like

$$F(q) = \int \rho(\vec{r}) e^{i\vec{q}\cdot\vec{r}} d^3 r$$

$$= \frac{4\pi}{q} \int_r r\rho(r)\sin(qr)\,dr \tag{2.20}$$

For SI interactions a starting approximation can be obtained by using the Fourier

transform for a solid sphere, representing an interaction with the whole nucleus. For SD

interactions we use a thin-shell approximation, representing an interaction with the outer

most unpaired nucleon.

Thin Shell (SD):

$$F(qr_n) = j_0(qr_n) = \frac{\sin(qr_n)}{qr_n} \tag{2.21}$$

Solid Sphere (SI):

$$F(qr_n) = \frac{3}{qr_n} j_1(qr_n)$$

$$= \frac{3}{(qr_n)^3} \left[\sin(qr_n) - qr_n \cos(qr_n) \right] \tag{2.22}$$

where r_n is an effective nuclear radius approximated by $r_n = a_n A^{1/3} + b_n$. A more detailed

calculation of the SD form factor uses detailed nuclear shell model calculations, see

[60][61].

SI form factors are derived using the charge distributions experimentally

determined using scattering data from electrons and muons. The form factor proposed by

Helm [62] gives a useful analytic form for $F(qr_n)$

$$F(qr_n) = 3\frac{j_1(qr_n)}{qr_n}e^{-(qs)^2/2} \tag{2.23}$$

where s is the nuclear skin thickness which has been observed to be essentially constant

[63]. Parameters in Eq. (2.23) are determined by experimental estimates of r_{rms}

$$r_{rms}^2 = \frac{3}{5}r_n^2 + 3s^2 \tag{2.24}$$

where

$$r_n^2 = c^2 + \frac{7}{3}\pi^2 a^2 - 5s^2 \tag{2.25}$$

and $c \cong 1.23A^{1/3} - 0.60\,fm$ are used in Fig. 17.

Another approximation is obtained using the Fermi distribution for charge

$$\rho(r) = \rho_0 \left[1 + e^{\frac{r-c}{a}}\right]^{-1} \tag{2.26}$$

and numerical integration. See Fig. 17 for a comparison of each these approximations

using Na and I.
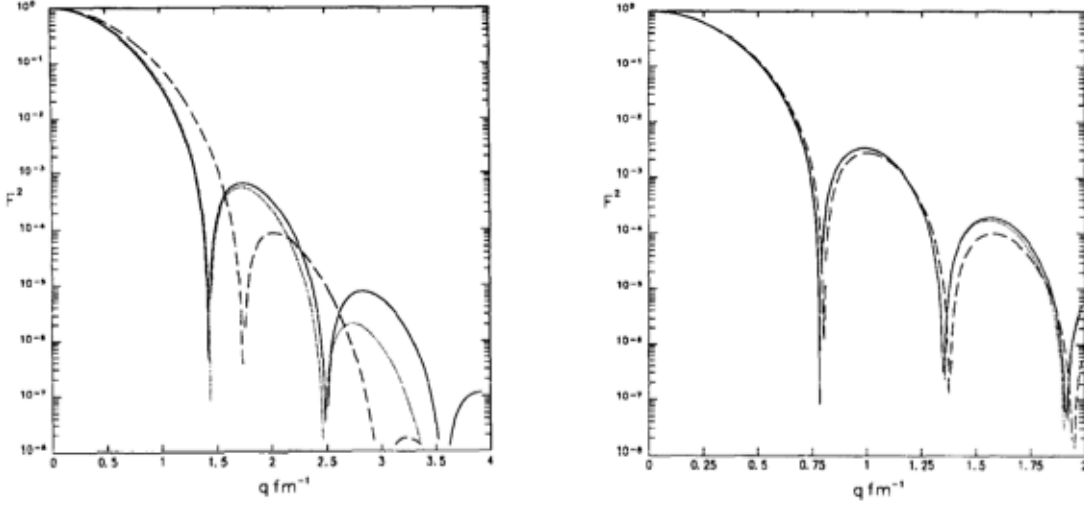
Fig. 17. F(q) vs q for Na (left) and I (right). Numerical solution using Fermi Density and Fricke data (solid) [63]; Helm Density using Eq. (3.24) and Eq. (3.25), with s = 0.9 fm (dots); Helm density using r_{rms}= 0.93$A^{1/3}$, with s = 1.0 fm (dashes) [60]. (Fig. from [59])

2.2.3 Interaction Factor

The last component in Eq. (2.6) is the interaction factor that is dependent on the spin-component of the target nucleus. The zero-momentum WIMP-nucleus cross section from Eq. (2.8) is

$$\sigma_0 = 4G_F^2\mu^2 I \qquad (2.27)$$

where G_F is the Fermi coupling constant and $\mu = {M_T M_\chi}\big/{(M_T + M_\chi)}$ is the reduced mass.

[57] I is different for spin-independent, I_{SI}, and spin-dependent, I_{SD}, interactions. For the spin-independent case

$$I_{SI} = \frac{1}{\pi G_F^2}\left[Zf_p + (A-Z)f_n\right]^2 \qquad (2.28)$$

where f_p and f_n are the effective WIMP-proton and WIMP-neutron couplings. For a Majorana WIMP they are approximately equal, simplifying Eq. (2.28) to

46

$$I_{SI} = \frac{1}{\pi G_F^2} \left(A f_p \right)^2 \quad \alpha \quad A^2 \tag{2.29}$$

As was mentioned earlier in Section 2.2.2, coherence is lost as the momentum

transfer increases ($qr_n \geq 1$) because the scattering amplitudes no longer add in phase.

Then the form factor must be used to get the correct event rate.

The spin-dependent case is slightly more complicated because the scattering

amplitude changes sign with spin-direction. So instead of adding together, the

amplitudes cancel each other out. Only the unpaired nucleons, nucleons with odd

numbers of protons and/or neutrons, have spin-dependent cross-section components.

$$I_{SD} = \frac{8}{\pi} \lambda^2 J(J+1) \tag{2.30}$$

$$\lambda = \frac{1}{J} \left[f_p \langle S_p \rangle + f_n \langle S_n \rangle \right] \tag{2.31}$$

where J is the total nuclear spin, λ is the spin coupling term, and $\langle S_n \rangle$ and $\langle S_p \rangle$ are the

spin expectation values of the nucleus [57].

2.3 Direct Detection Experiments

Direct detection searches for DM measure the elastic recoil of an incident WIMP

on a target nucleus. The extremely small interaction rates and low energy interactions

that were calculated in Section 2.2 means that an experiment must have specific

attributes if they are to detect such an interaction. The mass of the target material must

be large in order to have a detectable rate of scattering interactions. It must constructed

be of ultra-radio pure material and placed in a low background environment to reduce

background contamination of the signal as much as possible. SI interaction rates are proportional to A^2 and the SD interactions require a nucleus with nonzero nuclear spin, this means the target material needs to have an odd number of nucleons and have a large mass. There are a number of direct detection experiments currently underway that fit this profile. Only a couple of these will be elaborated on here, specifically those showing evidence for low-mass (<20GeV) WIMPs.

2.3.1 DAMA/LIBRA

The DAMA/LIBRA [64] experiment is investigating the model independent Dark Matter annual modulation signature using a NaI(Tl) detector array. They are located underground at *Laboratorio Nazionali della Gran Sasso* (Gran Sasso National Laboratory) in Italy and use 25 (9.7kg) highly pure thallium doped sodium iodide crystals coupled to 2 low background PMTs working in coincidence to study these interactions. They calibrate with X-rays and γ-rays down to a few keV and have optimized their detector for low energy event detection. The cumulative results for DAMA/LIBRA and DAMA/NaI [65] were published in 2010 consisting of 1.17(ton x yr) of exposure over 13 annual cycles. The single hit (one recoil in a single crystal) residual rates were fitted to a cosine function with the form $A\cos(\omega(t-t_0))$ with a period of $T = 2\pi/\omega = 1yr$ and a phase of 152.5 days (June 2nd). The results shown in Fig. 18 show a clear cosine-like modulation for the single hit events. The measured period is 0.999 ± 0.002 yr and phase is 146 ± 7 days at 8.9σ C.L. The modulation is present in the single hit events but not the multiple hits events and only in the 2-6 keV energy intervals not in any higher regions. So far there have not been any systematic or side processes

located that will satisfy all the peculiarities of the signature, and account for the whole

modulation amplitude.
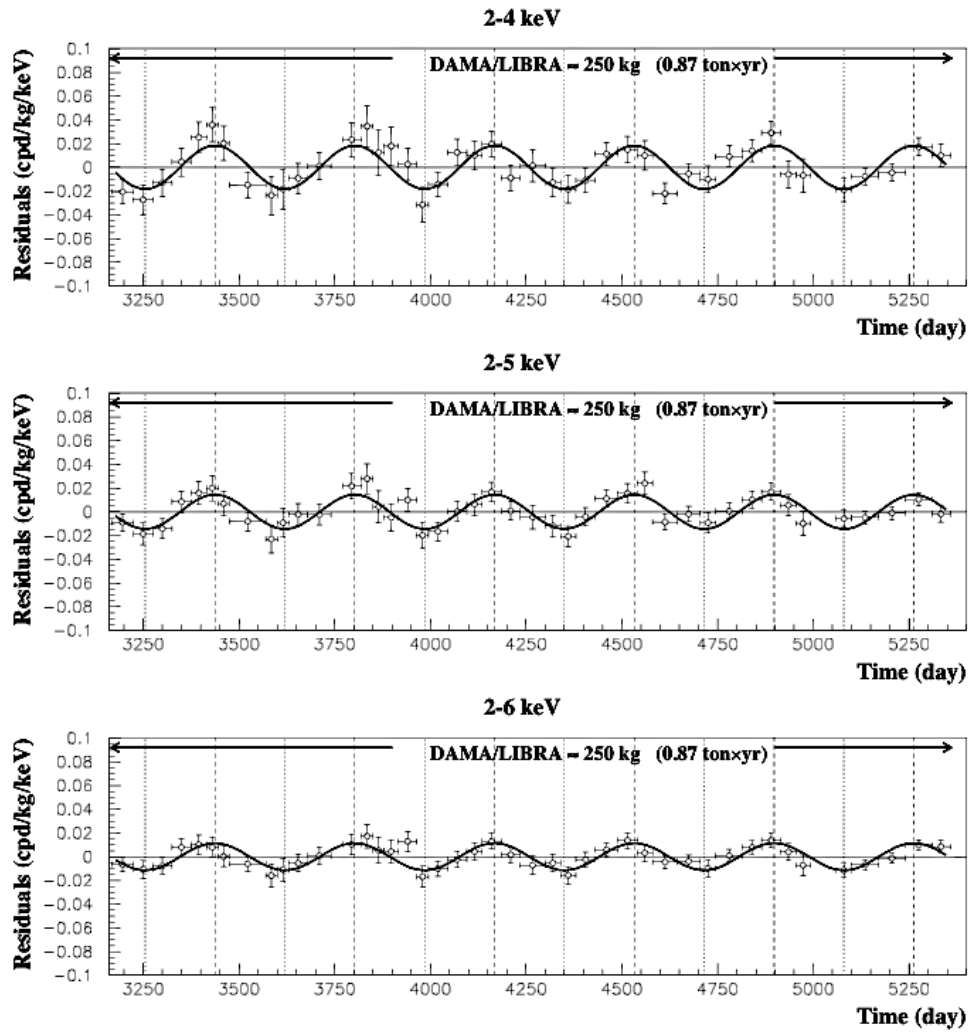
Fig. 18. The combined DAMA/LIBRA and DAMA/NaI experimental results. Data points are model-independent residual rate of single-hit scintillation events in the (2-4), (2-5), (2-6) keV energy intervals. The time scales start at Jan 1st of the first year of data taking for the DAMA/NaI detector. Overlaid curves are the cosine function annual modulation fit. The dashed vertical lines are the maximum expected for a DM signal and the dotted vertical lines are the minimum. (Fig. from [65])
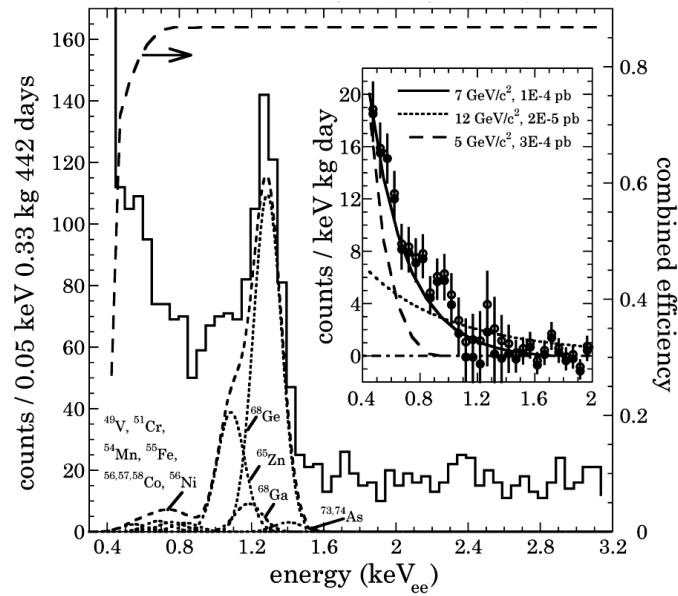
Fig. 19. CoGeNT low energy spectrum after all surface event cuts. Dotted Gaussian peaks show the predicted L-shell and electron capture contributions. Inset: Spectrum after L-shell contribution removed and flat background cuts. Predicted WIMP signals for several masses overlaid. (Fig. from [67])

2.3.2 CoGeNT

The CoGeNT detector is a p-type point contact (PPC) germanium detector located underground at the Soudan Underground Laboratory in Minnesota. PPC's have the useful combination of high mass crystals with low electronic noise that make them ideal for low-energy events. The CoGeNT collaboration has published results from 15 months of data using 440g PPCs showing an exponential-like irreducible background of events that took place in the bulk of their detector consistent with a low-mass WIMP (See Fig. 19) [66]. CoGeNT has also published results for an annual modulation signature, Fig. 20. A modulation is observed in the same region as the irreducible
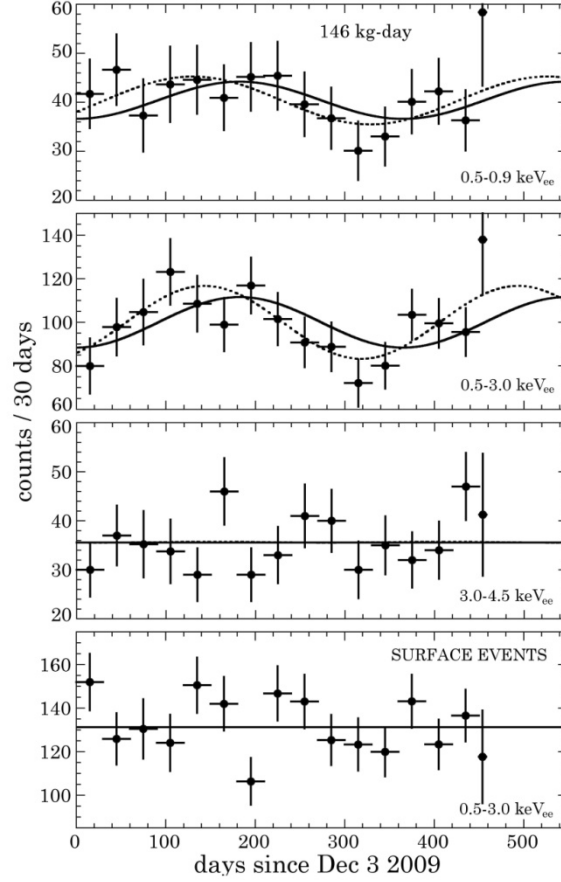
Fig. 20. CoGeNT modulation signature over (0.5-0.9), (0.5-3.0), and (3.0-4.5) keVee energy ranges. The lowest plot is of surface events over (0.5-3.0) keVee. The last bin spans 8 days. Dotted line: best-fit modulation. Solid line: nominal predictions from light WIMP hypothesis. (Fig. from [67])

exponential background at 2.8σ C.L. The best-fit values for their modulation parameters are 16.6 ± 3.8 % modulation amplitude, period of 347 ± 29 days, and a minimum at Oct. 16 ± 12 days [67].

2.3.3 CRESST

The CRESST experiment look for WIMPs via their elastic scattering off nuclei. They published results in Sept 2011 for 730 kg days of running for eight 300g $CaWO_2$ crystals [68]. Their detector crystals are operated at cryogenic temperatures of ~10mK in
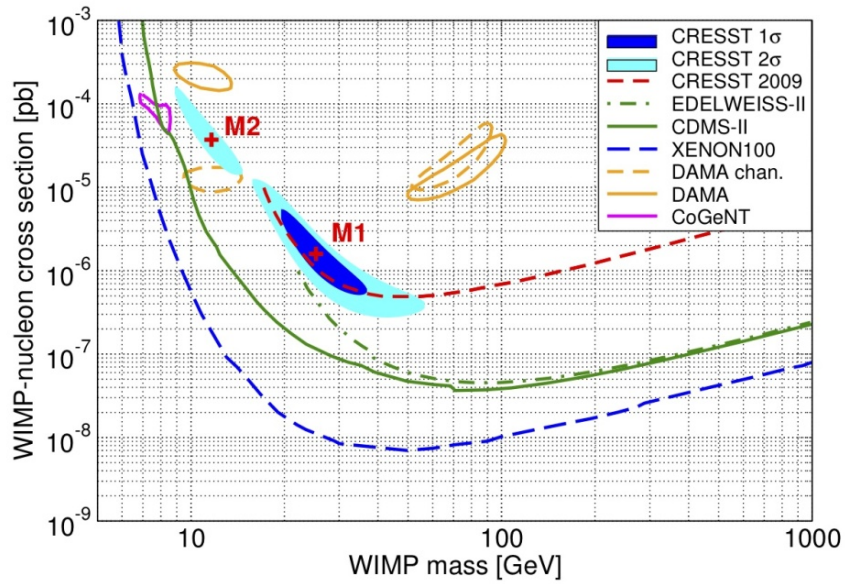
Fig. 21. The WIMP parameter space compatible with CRESST results [68]. M1 corresponds to a 25.3 GeV WIMP and M2 to a 11.6 GeV WIMP. Also shown are exclusion limits from CDMS-II [69], XENON100 [70], and EDELWEISS-II [71]. The magenta and gold regions are 90% C.L. from CoGeNT [67] and DAMA/LIBRA [64]. (Fig. from [68])

the Gran Sasso National Laboratory in Italy. The energy deposited into a crystal from an interaction is mostly converted into phonons, which are detected by a tungsten transition edge sensor (TES). The TES is a thin tungsten film evaporated onto the crystal then held at the transition temperature for superconductivity. Using a standard isothermal WIMP halo model they find two maxima within their likelihood function, M1 at 4.7σ and M2 at 4.2σ (See Fig. 21). The first corresponds to a 25.3GeV WIMP, the second is a 11.6GeV WIMP.

2.3.4 CDMS II

The Cryogenic Dark Matter Search (CDMS) collaboration is searching for nuclear recoils from WIMPs in semiconductor detectors operated at very low temperatures, ~4 mK. CDMS-II is located at the Soudan Underground Laboratory. The

Ge and Si detectors measure ionization and out-of-phase phonons. In April 2013 they published results from eight Si detectors with a total exposure of 140.2 kg-days [69][72]. There are three possible WIMP-like candidate events observed and an expected background of only 0.41 events. They calculate that there is a 5.4% likelihood of these events being a statistical fluctuation of background. The best fit for the data is a WIMP mass of 8.6 GeV/c^2, Fig. 22, and a 90 % upper confidence limit on the WIMP-nucleon cross section of 2.4 x 10^{-41} cm^2 at a WIMP mass of 10 GeV/c^2.
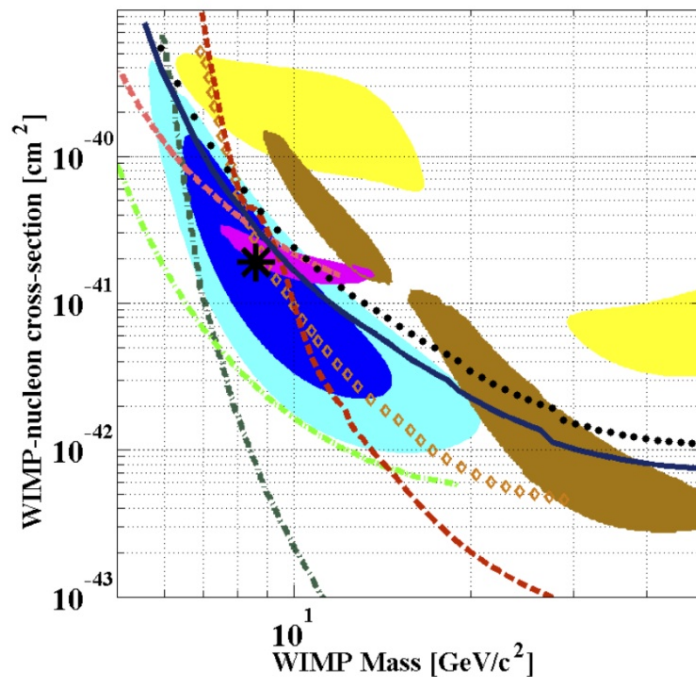
Fig. 22. CDMS II experimental upper limits (90% C.L.) for the WIMP-nucleon spin-independent cross section as a function of mass [69]. CDMS II Si analysis in [72] (black dots), combined with CDMS II Si data (solid blue), CDMS II Ge standard and low threshold (dark and light dashed red), EDELWEISS low-threshold (orange diamonds), XENON10 S2-only (light dashed-dotted green), and XENON100 (dark dashed-dotted green). Filled regions are possible signal regions from CoGeNT (magenta, 90% C.L.), DAMA/LIBRA (yellow, 99.7% C.L.) and CREEST (brown, 95.45% C.L.). CDMS II Si analysis is (blue, 68% C.L.) (cyan, 90% C.L.). Maximum likelihood point at 8.6 GeV/c^2 and 1.9 x 10^{-41} cm^2 (black asterisk). (Fig. from [72])

Based on indications of dark matter detection by these experiments it is clear that understanding the performance of such detectors at very low nuclear recoil energies (few keV) is key. In the sections which follow we will describe the measurements we have performed on a thallium doped sodium iodide detector to characterize its response to low energy nuclear recoils.

3. NaI(Tl) DETECTORS

Thallium doped sodium iodide is a popular choice of inorganic crystal scintillator. It has a high light yield and pulse shape discrimination between electron and nuclear recoils. The NaIAD [73], ELEGANT-V [74], ANAIS [75], and DAMA/LIBRA experiments are just a few of the groups who have utilized NaI(Tl) crystals in DM searches. NaI(Tl) is of particular interest because ^{23}Na and ^{127}I have nuclear spin, making them sensitive to SD interactions. In order to derive DM counting rates it is necessary to know the absolute efficiency of nuclear recoil energy to scintillation photons. This ratio is called the quenching factor (QF) and this section we discuss the quenching factor as it applies to NaI(Tl) and the current experimental measurements at low nuclear recoil energies.

3.1 Calculating the Quenching Factor

It's well known that the scintillation response to nuclear recoils is less than the light yield of electron recoils, resulting from a γ-ray interaction of the same energy. This is called ionization quenching. After a nuclear collision, a recoiling nucleus looses energy through collisions with electrons and with other nuclei. Scintillators like NaI(Tl) are sensitive to the electronic energy loss but not to the non-radiative, or nuclear energy losses. The energy of an electron recoil that shows the same light output as the nuclear recoil is defined as the electron equivalent energy of a nuclear recoil (keVee). The quenching factor is dependent on the rate of energy loss (dE/dx) and is defined as the ratio of the nuclear recoil response to the electron recoil response.

55

$$QF = \frac{E_{nr}}{E_{ee}} \qquad (3.1)$$

The Lindhard theory [76][77] attempts to quantify the energy loss from first principles in an attempt to theoretically determine the quenching factor. The idea is to first rescale the range or total distance traveled by the particle inside the scintillator, x, and the energy deposited, E_x, of the recoiling nucleus to dimensionless variables, ρ and ε. The nuclear energy loss is defined as a universal function that can then be calculated numerically, with

$$f_n(\varepsilon) = \left(\frac{d\varepsilon}{d\rho}\right)_n \qquad (3.2)$$

for the nuclear energy loss and

$$f_e(\varepsilon) = \left(\frac{d\varepsilon}{d\rho}\right)_e = \kappa\sqrt{\varepsilon} \qquad (3.3)$$

for electronic energy loss. When the recoiling atom is the same as the medium (for a material containing only one type of atom) then,

$$\varepsilon = \frac{11.5}{Z^{7/3}} E_x$$
$$\kappa = \frac{0.133}{\sqrt{A}} Z^{1/12} \qquad (3.4)$$

where Z is the atomic number of the target nuclei, A is the mass number of the target nuclei and E_x is the energy deposited in keV [77]. If the electronic and nuclear collisions are uncorrelated then the total energy deposited can be split up into energy deposited into atoms, η, and energy deposited into electrons, ν. The total energy is then

$$\varepsilon = \eta + \nu \qquad (3.5)$$

56

The electronic energy can be approximated using [59]

$$v = \frac{\varepsilon}{1 + \kappa g(\varepsilon)} \tag{3.6}$$

$$g(\varepsilon) = 3\varepsilon^{0.15} + 0.7\varepsilon^{0.6} + \varepsilon$$

The quenching factor is then the nuclear energy deposited divided by the total energy deposited. Using Eq. (3.5) and Eq. (3.6) gives

$$\frac{\eta}{\varepsilon} = \frac{\kappa g(\varepsilon)}{1 + \kappa g(\varepsilon)} \tag{3.7}$$

See Fig. 23 for a graph of Eq. (3.7) for sodium in sodium, and iodine in iodine. This approximation only holds for the recoiling atom being the same as the medium. The calculation of sodium in iodine is significantly more complicated and the above calculations can't be used.

In semiconductors the signals from ionization agree well with the Lindhard model, which means all the energy given to electronic collisions is visible. This is not the case with solid scintillators like NaI(Tl). Measurements show that a much smaller value is observed than Eq. (3.7) predicts. This means that there is some degree of electronic quenching as well as the nuclear quenching. [78]

Another approach to approximating the quenching factor is proposed by J.B. Birks in [79]. His is a semi-empirical approach that says the light yield of a scintillating material is dependent on the energy of the particle and the total stopping power
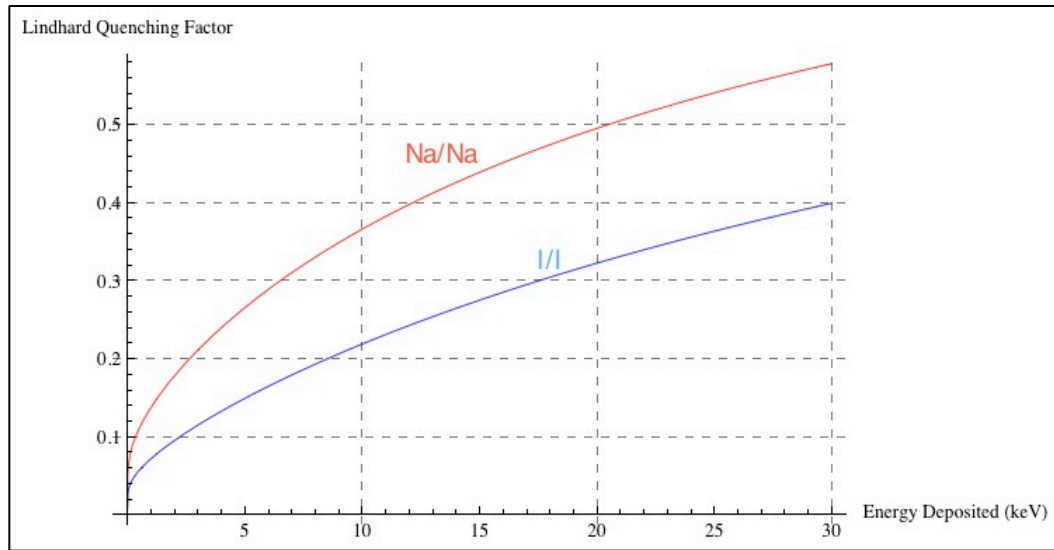
Fig. 23. The theoretical curves for the quenching factor of sodium and iodine recoils. The red curve represents sodium in sodium and the blue curve represents iodine in iodine.

in the material. For highly ionizing particles like protons, alphas and nuclear recoils Birks proposes the quenching factor for ions is the light yield for ions divided by the light yield for electrons of the same energy.

$$Q_i(E) = \frac{\int_0^E \dfrac{dE}{1 + kB\left(dE/dx\right)_i}}{\int_0^E \dfrac{dE}{1 + kB\left(dE/dx\right)_e}} \tag{3.8}$$

where kB is defined as the Birks factor and dE/dx is the total stopping power of the ions or elections. It is not, as is often assumed, a universal constant but depends on experimental conditions such as temperature, amount of thallium doping, and the timing of signal collection. This makes the Birks approach difficult to compare experiment to experiment, and therefore should be used cautiously and only as a prediction. See Fig. 24 for an

58
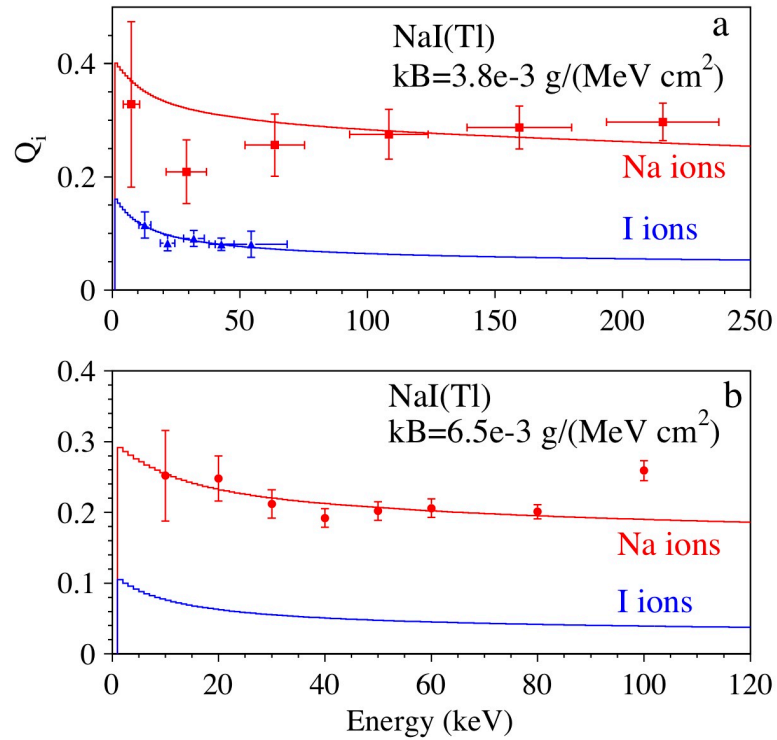
Fig. 24. Quenching factors for Na ions (•) in NaI(Tl) compared with Eq. (3.8) from the Birks approximation. (a) Points measured by Tovey *et al.* [80] and solid curve calculated using kB = 3.8 x 10^{-3} g/MeV/cm^2. (b) Points measured by Chagani *et al.* [81] and solid curve calculated using kB = 6.5 x 10^{-3} g/MeV/cm^2. (Fig. from [82])

example of the Birks approach using Eq. (3.8) overlaid onto current experimental results

from Tovey *et al.* [80] and Chagani *et al.* [81].

3.2 NaI(Tl) Scintillation Response

The early studies of NaI(Tl) made it clear that the scintillation light yield was

non-linear and also non-proportional to the energy deposited in the crystal. They further

were able to show that the resolution of the crystal based on the number of scintillation

photons produced did not follow the resolution predicted by Poisson statistics. The

crystal resolution is instead wider due to an unknown intrinsic resolution [83] [84] [85] [86]. Multiple studies have focused on quantification of the intrinsic energy resolution and measurement of the non-proportionality of the light yield for NaI(Tl) [87] [88] [89] [90] [91]. In the study by Khodyuk *et al*. [91] the non-proportional response (nPR) and energy resolution of NaI(Tl) was measured using highly monochromatic synchrotron radiation from 9-100 keV. In Fig. 25 their measured photon-nPR at an energy range $E_\gamma =$ 10-100 keV is plotted relative to the response at $E_\gamma = 662$ keV in percent. The shape of the photopeak-nPR is similar to other results [88]. The section that we are the most interested in will be from 9keV-30keV where the response increases from 111.5%-117.2%, a change of 5.7%. Fig. 26 shows a plot of the total energy resolution from [91] as a function of the number of photoelectrons. The plot spans 9 keV – 100 keV with resolution values starting at 21.9% and falling to 6.7%.

The total energy resolution of NaI(Tl) has been determined to be due to the photoelectron statistics and an additional component, termed the intrinsic resolution, which is associated with the photon-nPR [84]. There are three things associated with the light yield non-proportionality that cause the intrinsic resolution: the cascade of X-ray and Auger electrons following photoelectric absorption, the full energy absorption of
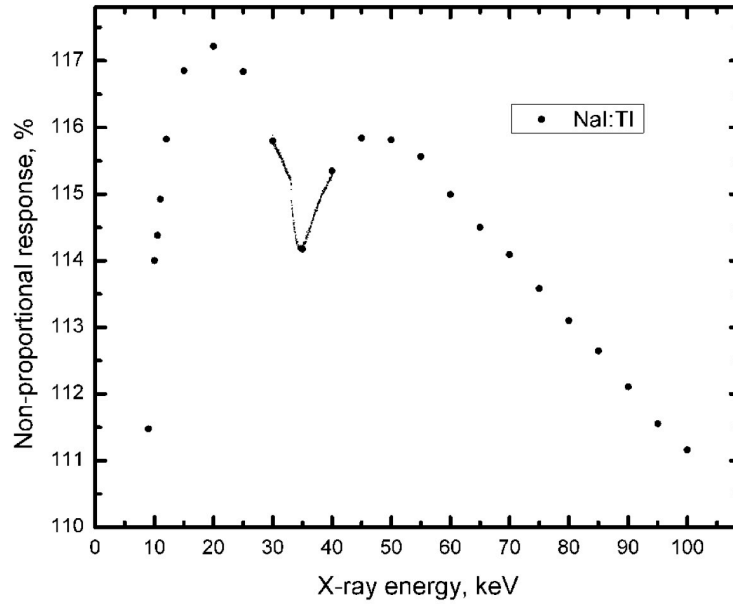
Fig. 25. Photon non-proportional response relative to NaI(Tl) crystal response at $E_\gamma = 662$ keV. X-ray energy in keV at 5 keV intervals. The dip in the nPR curve corresponds to the iodine K-shell binding energy. (Fig. from [91])
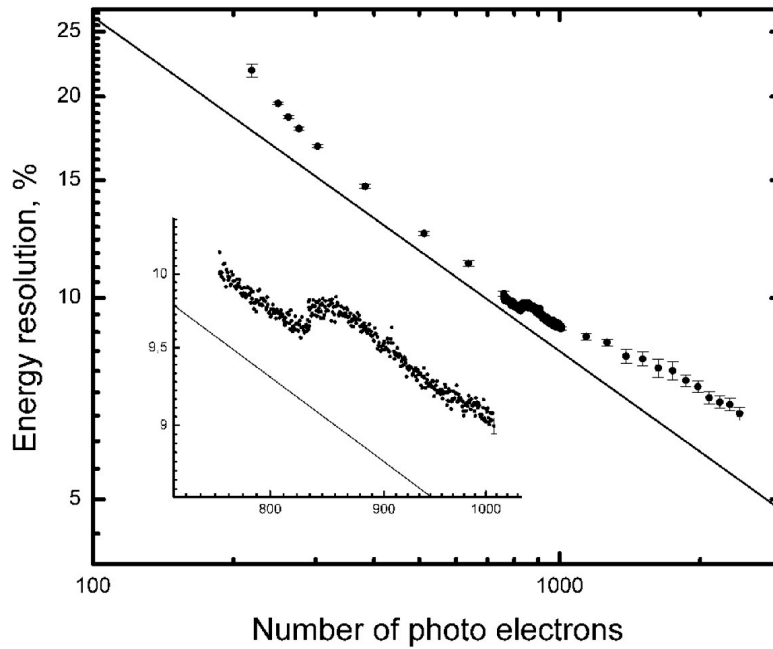
Fig. 26. Energy resolution of NaI(Tl) as a function of the number of photoelectrons detected. Solid line: R_{stat} calculated using Eq. (3.11). Inset: Close up of the resolution near the iodine K-shell binding energy. (Fig. from [91])

61

γ-rays following multiple Compton interactions, and the statistics related to the

formation of δ-rays [90]. The total resolution, R, can be written as

$$R = \sqrt{R_{stat}^2 + R_{np}^2}$$ (3.9)

where R_{stat} is the statistical resolution and R_{np} is the intrinsic resolution. An approximate

intrinsic resolution value can be calculated using a measurement of the energy resolution

of a γ-ray of known energy along with the statistical resolution due to the average

number of photons produced at that energy. The good approximation of the statistical

resolution is given by

$$R_{stat} = 2\sqrt{2\ln 2}\sqrt{\frac{1+\nu}{N_{spe}}}$$ (3.10)

where ν is the contribution from the variance in the PMT gain (≈ 0.25) and N_{spe} is the

average number of single photoelectrons detected. We use the electron capture peaks of

[128]I in Section 5.1 to do this calculation for our NaI(Tl) crystal.

3.3 Previous Quenching Factor Measurements

Quenching factors have been measured for NaI(Tl) by [80] [81] [92] [93] and

[94] to a minimum recoil energy of 10 keVnr. See Fig. 27 for a graph of their results

from 10 keVnr – 100 keVnr. It is clear that these measurements don't follow the

Lindhard curve prediction in shape or value. The solid line in Fig. 27 is a prediction

from Hitachi [78] which takes electronic quenching into account. It more closely

resembles the experimental values in shape and overestimates the quenching factor as

was expected in his calculations.

Because this is the energy range that the recoils of WIMPs are being reported it is of critical importance. The following experimental results will be compared to these and the simulated events using Geant4.
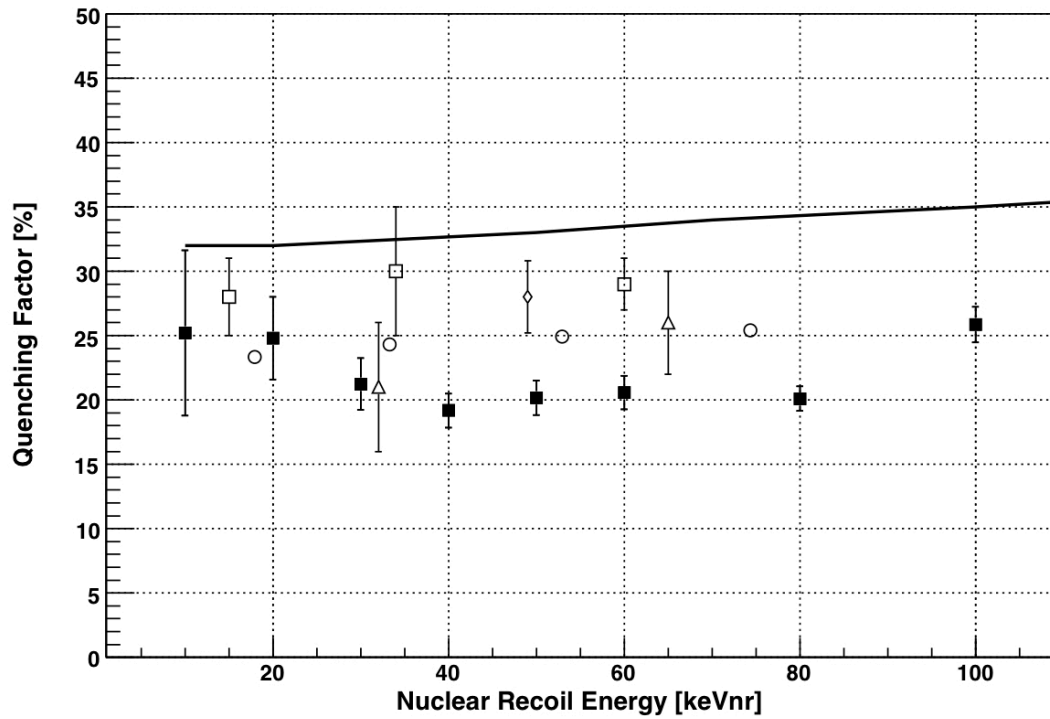

Fig. 27. Quenching factor for Na recoil in NaI(Tl) from past experiments. Experimental results from Chagani et al. [81] ■, Spooner et al. [93] □, Tovey et al. [80] Δ, Gerbier et al. [92] O, and Simon et al. [94] ◊. The solid black line is the Hitachi simulation for NaI(Tl) [78]. (Fig. from [81])

4. EXPERIMENTAL APPARATUS AND PROCEDURE

Our experiment investigates the low energy response of a single NaI(Tl) crystal using nuclear recoil response to low energy neutrons and induced radioactivity. We investigate energies relevant to low mass WIMPs searches. In order to measure the quenching factor, a 2" cylindrical NaI(Tl) crystal was exposed to a collimated mono-energetic neutron beam. Coincidences were recorded between neutrons scattering in the NaI(Tl) and then subsequently detected in the solid scintillating paddle detector positioned one foot away from the crystal, between the source and the NaI(Tl), to detect backscattered neutrons. The recoil energy in the target can then be calculated using Eq. (2.5) with $\theta = 180°$.

4.1 Detector at the Nuclear Science Center

The NaI(Tl) detector setup is located at the Nuclear Science Center at Texas A&M University, where we utilize the 2 MeV Pellitron Tandem accelerator to produce mono-energetic protons with energies up to 4 MeV. See Fig. 28 for a top down view of the beam path and Fig. 29 for a close up of the experiment.

The duoplasmatron creates negative ions using a cathode filament inside a vacuum chamber surrounded by a magnetic field. The cathode produces electrons which initiate an arc, which ionizes small amounts of H_2 gas producing a plasma. An electric field draws the H^- ions out of the source, through a small hole, into the high vacuum where they are accelerated to approximately 22 keV of energy. These ions are then

64

focused down the beam line into the Pellitron, where they are accelerated toward a thin carbon foil through a potential difference given by the terminal potential voltage. When they pass through the carbon foil the electrons are stripped off, leaving just the H^+ nucleus (proton). The protons are then accelerated to the other side of the generator, doubling their energy, and passing through a set of focusing magnets to the experiment.
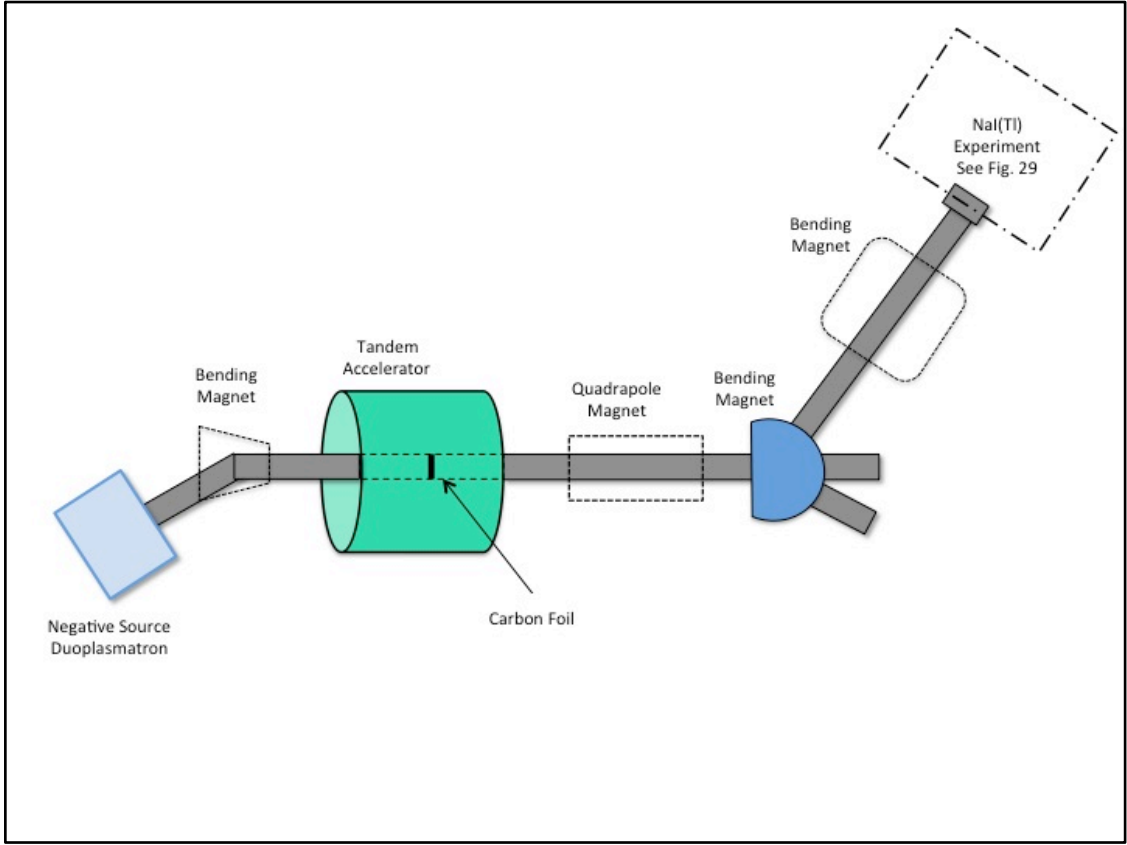
Fig. 28. Top-down schematic of the beamline at the nuclear science center.
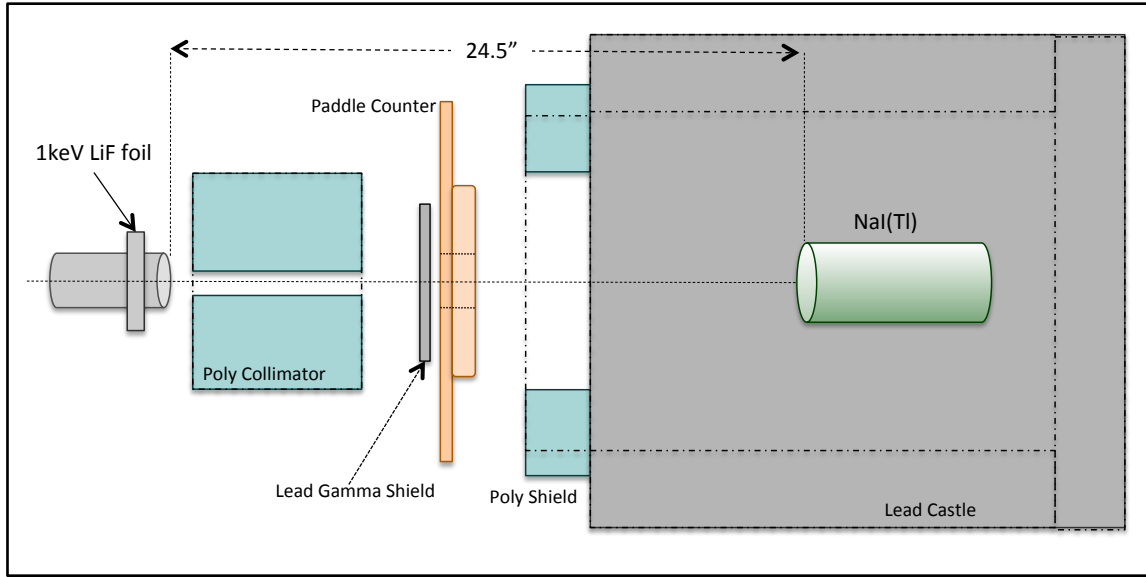
Fig. 29. Neutron scattering apparatus setup.

4.2 Neutron Production

4.2.1 The $^7Li(p,n)^7Be$ Reaction

The neutrons are produced using the $^7Li(p,n)^7Be$ nuclear reaction. Protons from the accelerator are incident onto a LiF coated target. The neutrons are then emitted with an energy

$$E_n = E_p \frac{m_p m_n}{(m_n + m_r)^2} \left\{ 2\cos^2\theta + \frac{m_r(m_r + m_n)}{m_p m_n}\left[\frac{Q}{E_p} + \left(1 - \frac{m_p}{m_r}\right)\right] \pm 2\cos\theta\sqrt{\cos^2\theta + \frac{m_r(m_r + m_n)}{m_p m_n}\left[\frac{Q}{E_p} + \left(1 - \frac{m_p}{m_r}\right)\right]} \right\} \qquad (4.1)$$

where E_p is the proton energy, θ is the emission angle of the neutrons, m_p is the mass of the proton, m_n is the mass of the neutron and m_r is the mass of the residual nucleus (Be).

This is an endothermic reaction, with the experimental Q value of -1.644MeV [95], so

the reaction begins at a threshold energy given by

$$E_{ps} = |Q| \frac{m_p + m_t}{m_t} = 1.881 \text{ MeV}$$ (4.2)

where m_t is the mass of the target nucleus (Li). At the threshold energy the neutrons are

produced with zero energy in the center of mass frame. In the lab frame they move in a

forward peaked cone with energy

$$E_{ns} = E_{ps} \frac{m_p m_n}{\left(m_n + m_r\right)^2} = 30 \text{ keV}$$ (4.3)

The apex angle of the emission cone is given by

$$\cos\theta_0 = \left| \sqrt{\frac{m_r \left(m_n + m_r\right)}{m_p m_n} \left[\frac{|Q|}{E} - \left(1 - \frac{m_p}{m_r}\right) \right]} \right|$$ (4.4)

Inside θ_0 there are two neutron energies, corresponding to the $\pm$ solutions in Eq. (4.1).

Each energy belongs to an emission angle in the center of mass frame. As the energy, E_p,

of the incident proton increases, the energy of one group increases and the other

decreases as the cone widens (Fig. 30). The energy of the second group goes to zero

when $\theta_0 = 90°$. This is called the mono-energetic threshold energy

$$E'_{ps} = |Q| \frac{m_r}{\left(m_t - m_n\right)} = 1.920 \text{ MeV}$$ (4.5)

For proton energies above this threshold, neutrons are produced in all directions and

only the + sign holds for E_n in Eq. (4.1). [96]

The energy of the neutron beam is calibrated using the "turn on" of the ${}^7\text{Li}(p,n){}^7\text{Be}$

neutrons in the NaI(Tl) detector. The energy of the terminal potential is slowly increased
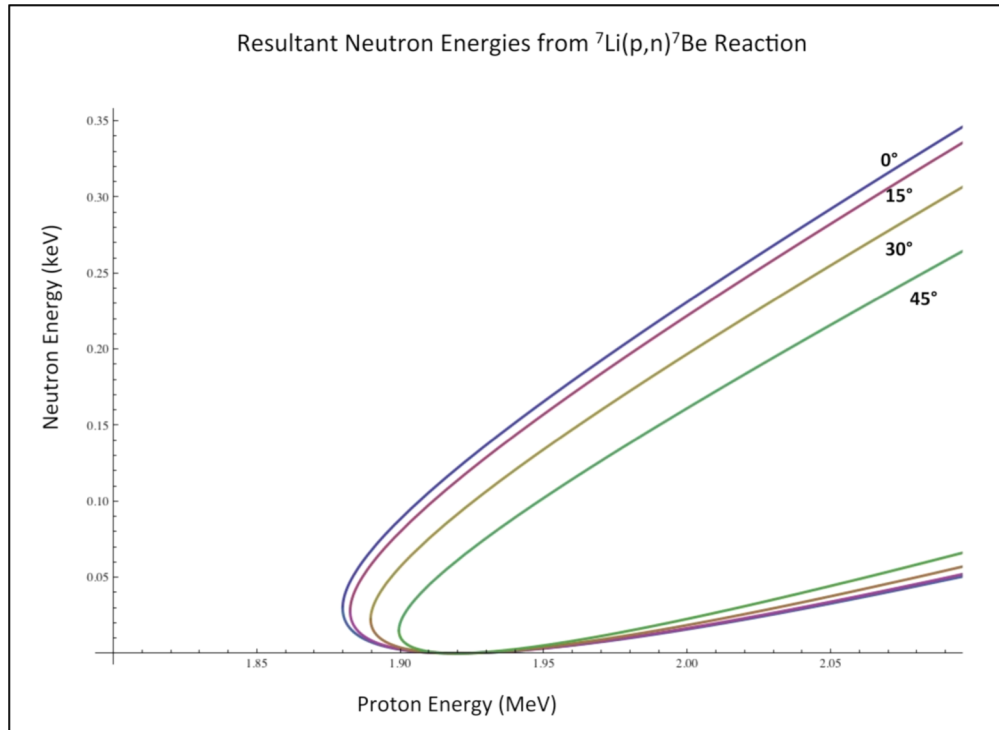
Fig. 30. Energy of the emitted neutrons vs incident proton energy at various emission angles near the threshold of the Li(p,n)Be reaction.

until neutrons are just detected, the bending magnet reading just below this value is set as the turn on value and associated with E_{ps}=1.881. The relationship between the magnitude of the magnetic field in the bending magnet and the proton energy is

$$E = aB^2 \tag{4.6}$$

Once the threshold energy and magnet settings are measured, then the constant can be calculated and the energy of the subsequent events determined. Typical constant values for our experiment range from $a = 24\text{-}26$.

4.2.2 Coating the LiF Foil

The LiF target was made using physical vapor deposition (PVD) via vacuum evaporation. Vacuum evaporation is a PVD process in which material from a thermal vaporization source reaches the substrate without colliding into other gas molecules in the intervening space [97]. The trajectory of the vaporized material is "line of sight". See Fig. 31 for a diagram of our coating chamber and relevant measurements. The mean free path in a vacuum for LiF is 5 cm at 10^{-3} torr and 5,000 cm at 10^{-6} torr. For a chamber 6"$\varnothing$ x 15" high, a vacuum of 10^{-5} torr should sufficiently reduce collisions to allow a coating to be deposited uniformly. The thickness goal is about 1-2 keV for a proton of threshold level energy at the center of the coated surface. The substrate chosen was a thin piece of stainless steel 2"x2". To calculate how much LiF needs to be used for evaporation we use

$$LiF(g) = \frac{\Omega\, t}{SP} \tag{4.7}$$

where t is the thickness (MeV), Ω is the solid angle the LiF powder can evaporate into, and SP is the stopping power of LiF at the target proton energy. A cosine distribution is needed to calculate the thickness distribution of the film formed on a planer surface above the source.

$$\frac{dm}{dA} = \frac{LiF(g) \cdot SP}{\Omega} \cos\theta \cos\phi \tag{4.8}$$

where θ is the angle measured from the normal of the vaporizing surface and ϕ is the angle from a line from the source to a point on the substrate, $\phi = 0$ for our substrate.

The substrate boat blocks out all but 30° for the "line of sight" trajectory, which is a solid angle of $\Omega = \pi r^2$. The stopping power at $E_p = 1.881$ MeV is SP = 1.3 x 10^2 (MeV cm^2/g). Plugging this into Eq. 4.7 gives a starting amount of LiF ≈ 0.007g.

We used 7.5mg of LiF, a starting vacuum of 4.5x10^{-5} torr, and an applied AC voltage of 1.21V for 3 min. The final estimates place the foil thickness at 0.84 keV at the center of the stainless and 0.82 keV at the edge.
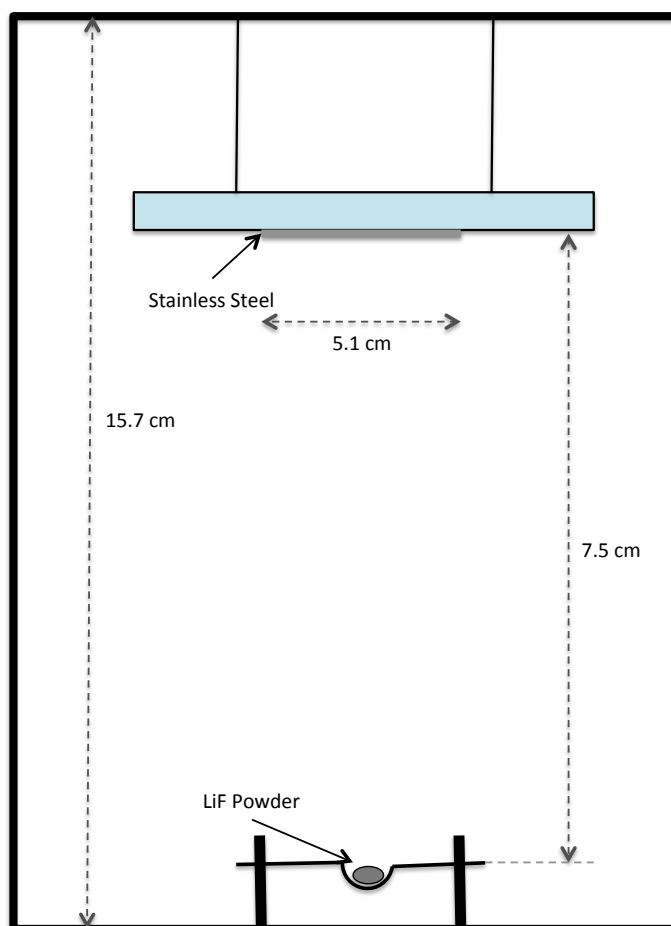

Fig. 31. Evaporation chamber for LiF coated stainless steel.

4.3 Monte Carlo Simulations

In order to accurately simulate the full spectrum of events in the NaI(Tl) crystal a Monte Carlo simulation was performed using the Geant4 framework [98]. The geometry in Fig. 29 was the final setup decided on after several different configurations were evaluated. The shielding was optimized for the highest flux of un-attenuated neutrons and lowest backgrounds from scattered neutrons. The neutron beam was simulated using the emission spectrum expected from Eq. (4.1). Fig. 32 shows examples of the produced neutrons at several energy ranges near the ^{7}Li(p,n)^{7}Be threshold. The two separate energy groups that were discussed in Section 4.2.1 are clearly visible.

The neutron energies in Fig. 32 represent the full 180° of possible emission angles. The energy of neutron beam that actually reaches the NaI(Tl) is shown in Fig. 33. The neutrons kinetic energy upon reaching the detector, after any collisions with shielding, air molecules, or the paddle counter are plotted over the original production energy. With this setup we attain approximately 90% un-attenuated neutrons near threshold.

The internal decay of neutron activated iodine is used to calibrate the scintillation response at low energies. The X-rays resulting from electron capture in ^{128}I, with appropriate Gaussian smearing of the energy, is also simulated using Geant4 and compared to real data. This is covered in more detail when energy calibration of the crystal is discussed in the next section.
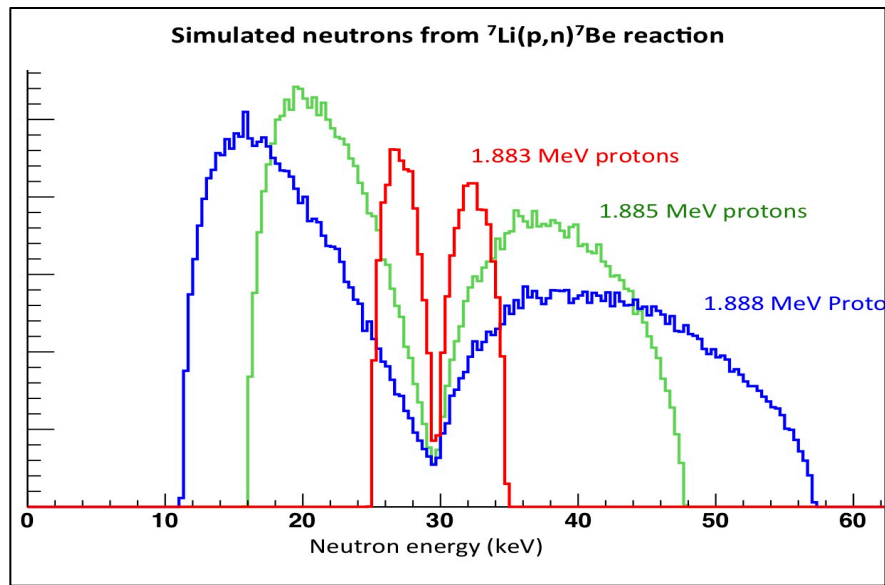
Fig. 32. Emitted neutron energy spectrum from the ^{7}Li(p,n)^{7}Be reaction for various initial proton energies. 1.883 MeV protons (red), 1.885 MeV protons (green), 1.888 MeV protons (blue).
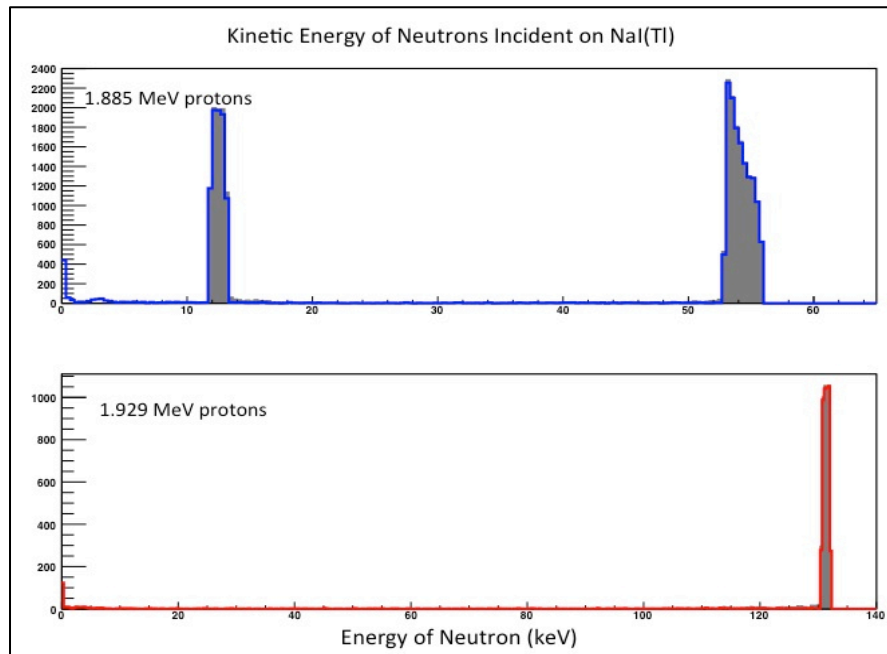
Fig. 33. Resultant neutrons from simulated experimental setup at two initial proton energies, above and below the mono-energetic threshold. Blue and Red lines: The kinetic energies of neutrons when they reach the NaI(Tl). Dark grey fill: The energy of the neutron at the source. Top: 1.885 MeV protons. Bottom: 1.929 MeV protons.

Another study was performed to obtain estimates for the percent of multiple-scattered neutrons inside the NaI(Tl) crystal. This is a background that is significantly reduced in our crystal due to its small size but is still an unavoidable background. The energy profile of these events has been mapped to facilitate background cuts in the actual data. Geant4 simulations show that approximately 27% of all events that deposit energy in the NaI(Tl) have more then one scattering of the neutron and 36% of coincidence events between the NaI(Tl) and the paddle counter result from multi-scattering of the neutron in the crystal. In Fig. 34 it's clear that the deposited energy spectrum for events with multiple recoils is featureless, where as the one for single scatter events contains a distinct energy threshold for backscatter neutrons. It will be this feature of our data that will allow us to study the energy dependence of these neutron scatters.

Fig. 34. Energy deposited (keV) into the NaI(Tl) crystal by recoiling neutrons produced from 1.915 MeV protons. Dark grey fill: Events with only one scattering of the neutron inside the crystal. Blue line: Events that have multiple scatters in the crystal. A clear backscatter cutoff is visible in the single scatters but not in the multi-scatter events.
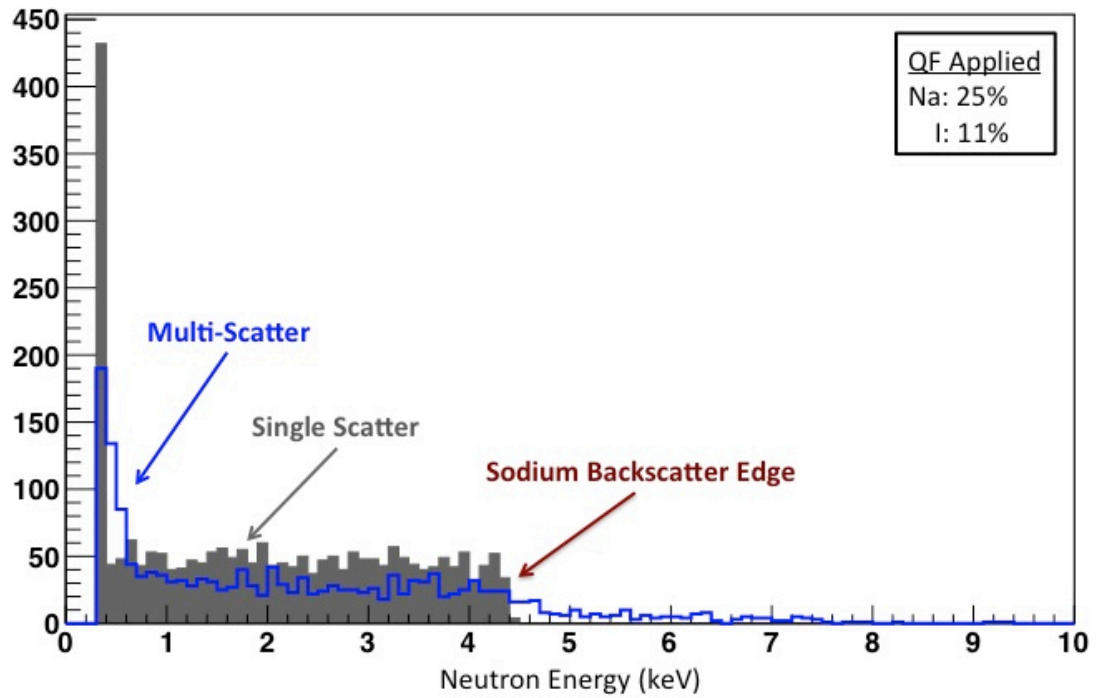
5. DATA ANALYSIS AND RESULTS

5.1 Electronics Chain and Event Selection

5.1.1 Electronics Hardware

Fig. 35 shows schematically the configuration of electronics for the experiment. The signal from the two paddle counter PMTs are added together and sent out to a channel of the data acquisition system (DAQ) and to a discriminator, which outputs to the coincidence trigger. The primary signal from the NaI(Tl) PMT is amplified and split, one is sent to the DAQ as the NaI(Tl) "fine signal". Another is sent through a 50 Ω splitter into a discriminator and a second DAQ channel as the NaI(Tl) "coarse signal". A third signal from the NaI(Tl) is further amplified and sent into a discriminator and a 150 ns delay generator. All three of the discriminator signals are sent to the coincidence trigger. The coincidence trigger can be used to select coincidences between the paddle and the NaI(Tl) with a 100 ns overlap, or it can be set as a self coincidence in the NaI(Tl). The DAQ signals are recorded with an Acqiris DC265 digitizer, a 500 MHz sampling rate and 2 ns sampling time. Each event records a total time of 5 μs, or 2500 samples. The data acquisition software reads out the digitized waveforms and saves them for later analysis offline.

5.1.2 Event Selection

A preliminary analysis program reads each event and records the amplitude for each 2 ns sampling point. A baseline is calculated for each event using a 400 ns window. The second set of cuts requires that no energy is deposited in the first 170 ns.

Fig. 35. Hardware trigger electronics chain for our experiment. Signals from the NaI(Tl) PMT and the paddle counter PMTs are amplified, split then sent to an input channel of the DAQ and through a discriminator. The discriminator signals are sent to the external trigger of the DAQ, which is set as a coincidence between the NaI(Tl) and the paddle or as a self coincidence in the NaI(Tl).
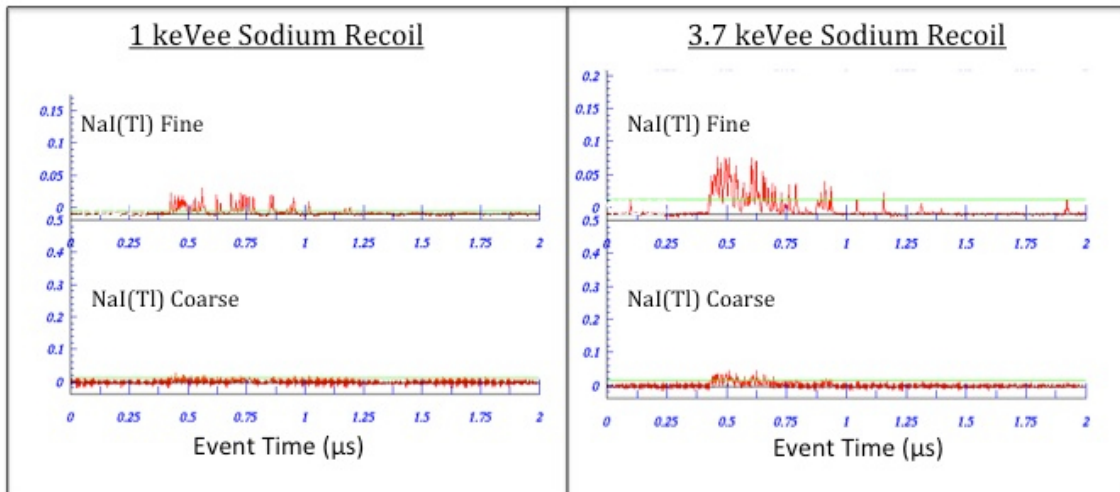
Fig. 36. Signals from a 1 keVee and 3.7 keVee nuclear recoil in the NaI(Tl) recorded with the Acqiris DC265 digitizer. Top: Fine scale NaI(Tl) channel. Bottom: Coarse scale NaI(Tl) channel.

This is to reduce so called "tail events", which are triggers on the low energy tails of much larger events. The tails are caused by the long decay time of NaI(Tl) scintillation pulses. Events must have 80% of their total energy between 170-350 ns and have a height to width ratio (pulse hight/pulse width) < 0.1cnts/ns. These two requirements isolate the signal and pick out only the "short wide" events which are characteristic of neutron recoils. See Fig. 36 for a sample of what these signals look like when processed with a waveform viewer. The top signal is the "Fine NaI(Tl)" channel and the bottom is the "Coarse NaI(Tl) channel.

5.2 Scintillation Response of Our Crystal

In order to correctly interpret our measurements, we need to fully understand the scintillation response of our particular NaI(Tl) crystal. First we need to determine the number of single photoelectrons (spe) produced per keV of energy deposited. The single photoelectron spectrum from our crystal is shown in Fig. 37. A Gaussian fit gives a mean area for a spe = 0.053 in arbitrary units for our PMT. Next we take the area for each event and divide by the area of a single photoelectron to get a value for the number of photoelectrons per event. Using the number of spes in an event with a known energy we can calculate the spe/keV. For a calibration energy we use the internal electron capture gammas from the iodine in the crystal. The ^{128}I becomes activated by the neutron bombardment during data taking and has a well measured half-life of $t_0 = 24.99$ min [99]. By taking a data run after the beam is turned off we can track the radioactive decay

Fig. 37. Single photoelectron response from NaI(Tl) PMT. Left: Total low energy response divided into single and double photoelectron gaussian peaks. Right: Single photoelectron peak with a gaussian fit, mean value of 0.053 in area units for the PMT.

Table 2 Electron capture X-ray energy and relative intensity for ^{128}I decay. Values from [99]

Electron Capture X-rays from ^{128}I Decay	
Energy (keV)	Relative Intensity (%)
3.335	0.118
3.759	0.33
3.769	3.00
4.030	1.80
4.069	0.20
4.121	0.33
4.302	0.53
4.572	0.23
27.202	21.7
27.472	40.0
30.944	3.60
30.995	7.00
31.704	2.03
31.774	0.31
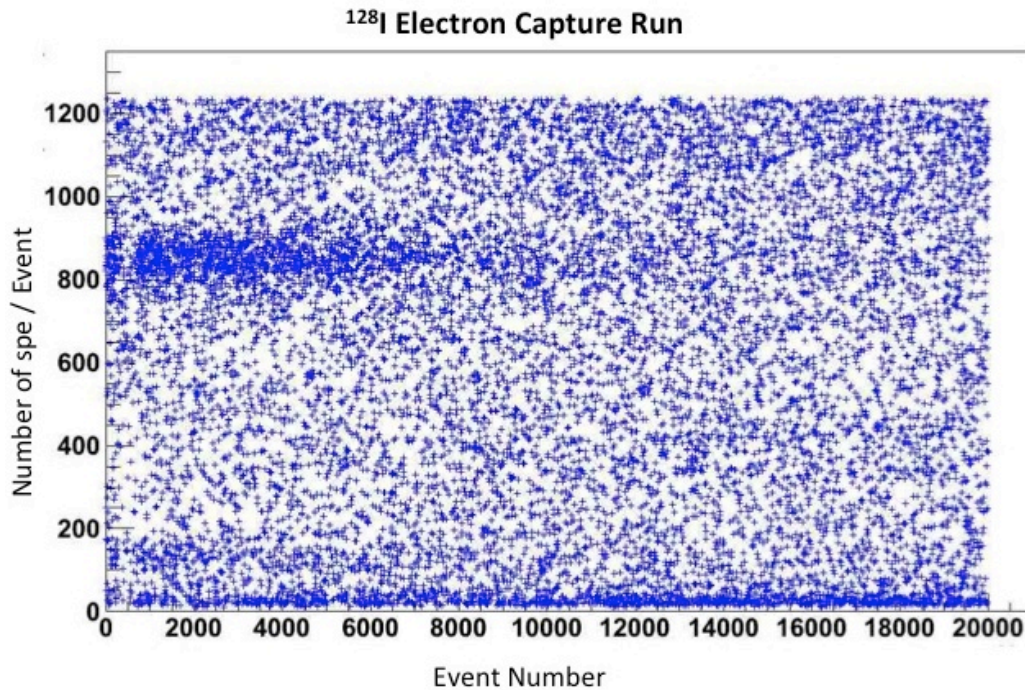
Fig. 38. Typical ^{128}I electron capture run from activated NaI(Tl) crystal. The number of single photoelectrons per event is plotted against the event number. The exponential decay of the rate is clearly visible for both the 4 keV and 27 keV peak.

of ^{128}I electron capture X-rays. Their energies and relative intensities are listed in Table 2.

If we record data with the neutron scattering setup after we stop the irradiation of the crystal, what we see are two Gaussian peaks that slowly decay away as time progresses. One is from the 3.769 keV and 4.03 keV lines, and the other from the 27.202 keV and 27.472 keV lines. The 4 keV peak will be approximately 8% as large as the 27 keV peak. Fig. 38 shows a graph of a typical e-capture run, the area is plotted vs event number. The time decay of the two peaks is clearly visible and a cut is made on the event number, which corresponds to the time, in order to maximize the peak height above

79
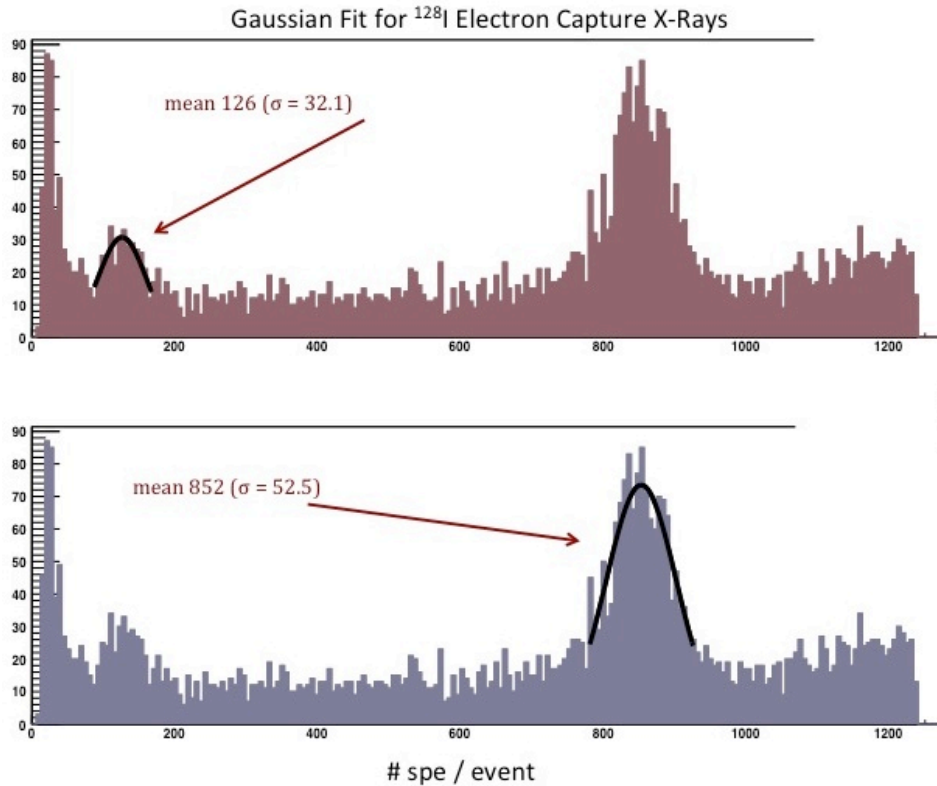
Fig. 39. Gaussian fit to ^{128}I electron capture X-rays in terms of the number of single photoelectrons per event.

background. The area of the remaining events is plotted and a Gaussian fit applied to the 2 observed peaks (Fig. 39). Once the two peaks have been fit with Gaussians the standard deviation for each gives a value for calculating the FWHM, 60% for the 4 keV peak and 14.5% for the 27 keV peak. The FWHM corresponds to the amount of smearing that needs to be applied to the simulated gamma spectrum using Geant4. The simulated X-ray spectrum uses the values in Table 2 and applies a Gaussian smearing to the energy of each gamma in order to simulate the crystal response to energy deposited. The number of photoelections per keV has a Gaussian shaped curve with a FWHM that corresponds to the crystal resolution at that energy. Because these are not mono-

energetic photons in each peak the FWHM is actually an overestimate of the crystal resolution. The simulation uses 60% for the X-rays near 4 keV and 14.5% for those near 27 keV. Geant4 calculates the X-ray energies with smearing, then runs those into a NaI(Tl) crystal. The resulting energy deposited values can be fitted to provide a mean kinetic energy expected from each decay peak. The mean value in spe is divided by the expected kinetic energy to obtain the spe/keV of our crystal. See Table 3 for the full set of results and uncertainties. We measured 32 spe/keV at 4 keV and 31 spe/keV at 27 keV. Note that the scale factor for the real data is different for the 4 keV peak and 27 keV peak. This means the crystals response increases as the energy increases over this interval as was discussed in Section 3.2.

The intrinsic resolution was calculated at 27 keV and combined with other experimental results from a similar NaI(Tl) crystal [100] in order to estimate the approximate resolution at lower energies (See Fig. 40). The intrinsic crystal resolution can be better determined by mono-energetic low energy gamma rays and could possibly improve the error bars with a more accurate measurement. This is not possible with our crystal due to its encapsulation in a sealed aluminum container.

Table 3 Relevant values and uncertainties for scintillation response calculations. Real data from a typical electron capture run and the simulated data from Geant4 gamma run.

Calibration Values for Scintillation Response Using Internal X-Rays		
	4 keV Peak	**27 keV Peak**
Real Data: 11k events from eCap Run (mean, sigma)	$\mu = 6.665 \pm 0.1317$ $\sigma = 1.689 \pm 0.1778$	$\mu = 45.10 \pm 9.519 \times 10^{-2}$ $\sigma = 2.782 \pm 0.1318$
FWHM from eCap Run	3.976 ± 0.419	6.550 ± 0.310
Experimental Resolution: R (% width from FWHM)	$59.66 \pm 7.46\%$	$14.52 \pm 0.72\%$
Gamma Simulation: using % smear (mean, sigma)	$\mu = 3.927 \pm 1.218 \times 10^{-2}$ $\sigma = 1.027 \pm 1.023 \times 10^{-2}$	$\mu = 27.55 \pm 9.547 \times 10^{-3}$ $\sigma = 1.813 \pm 9.871 \times 10^{-3}$
Crystal response: scale factor for real data (sim mean/real mean)	$0.5892 \pm 1.347 \times 10^{-2}$	$0.6107 \pm 1.501 \times 10^{-3}$
spe/keV for real data (real data/.053)/gamma mean	32.08 ± 0.7121	$30.92 \pm 7.285 \times 10^{-2}$
Calculated Statistical Resolution: R_{stat}	$23.45 \pm 0.23\%$	$9.021 \pm 9.5 \times 10^{-3}\%$
Calculated Intrinsic Resolution: R_{np}	-	$11.38 \pm 0.21\%$

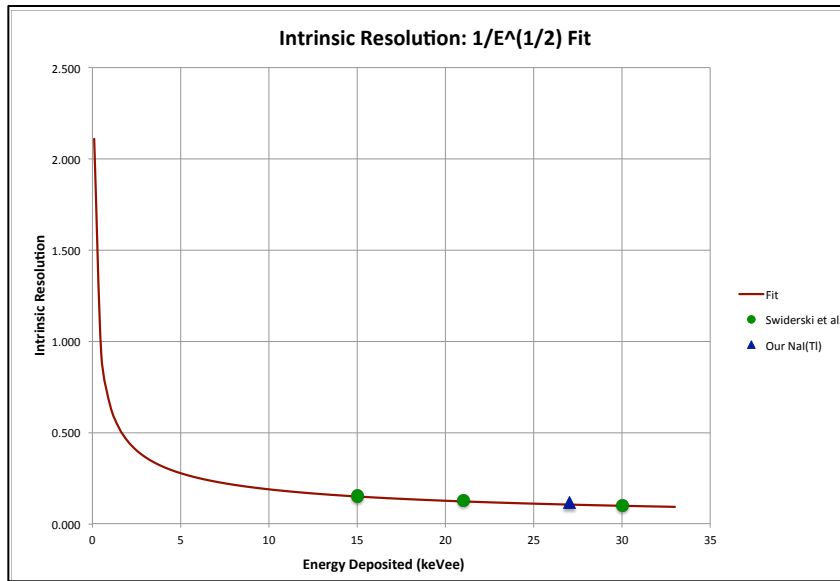**Fig. 40.** Approximate intrinsic resolution for NaI(Tl) crystal at room temperature. Blue triangle: This experiment. Green circles: Intrinsic resolution of a NaI(Tl) crystal measured by Świderski et al. [100]. Red line: $1/E^{1/2}$ approximate fit using 15 keV and 30 keV data points.
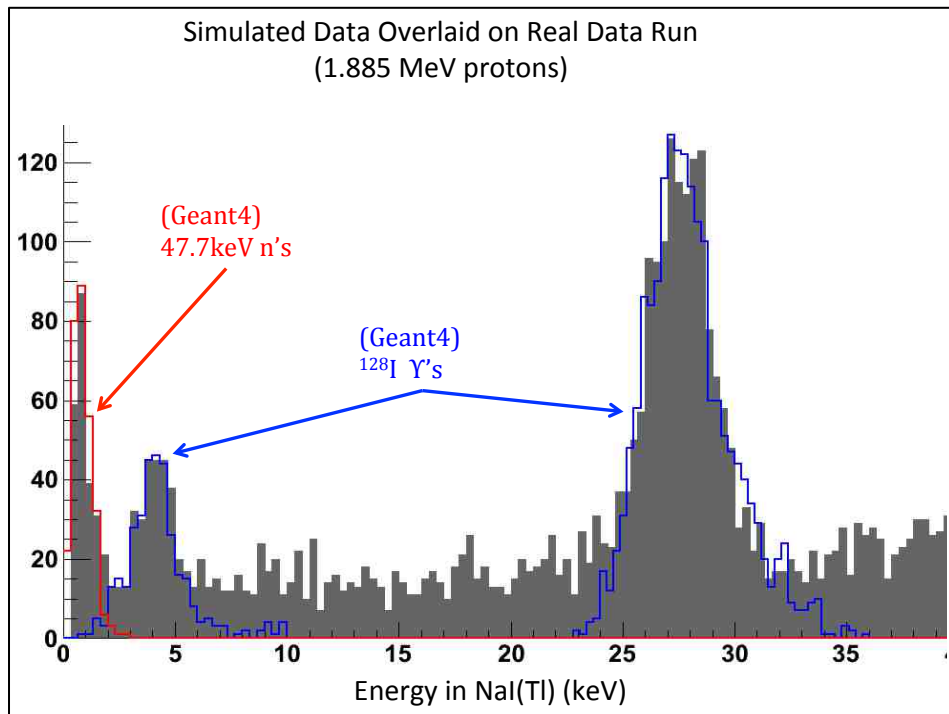

Fig. 41. Simulated gammas overlaid onto a real data set with 1.885 MeV proton beam. The neutron spectrum hitting the crystal is plotted in Fig. 33.

Putting everything together the simulated X-ray spectra with appropriate scale factors and smearing applied, the results are plotted with a low energy neutron run in Fig. 41. The NaI(Tl) crystal is very activated in this particular data set making the decay X-rays prominent. The neutrons are smeared according to the calculated R_{stat} and predicted R_{np} from the graph in Fig. 40. This lends further support to the intrinsic resolution curve at lower energies.

5.3 Quenching Factor Measurements

With the scintillation response of our NaI(Tl) crystal suitably characterized the quenching factor data sets can be analyzed. Starting at threshold for the ^{7}Li (p,n) ^{7}Be reaction and increasing in approximately 8-10 keV steps to Ep = 2.014 MeV, a series of data runs are made utilizing the setup depicted in Fig. 29. The self coincidence trigger of 150 ns on the NaI(Tl) is used with a lower threshold of 0.3 keV. At each energy 2,000 events were recorded and processed using the preliminary cuts discussed in Section 5.1.2. The analysis is then transferred to a ROOT platform [101] and the energy deposited for each event is plotted up to 40 keV. The scale factor obtained for the 4 keV escape peak is used to scale the energy deposited into keVee units (Table 3). Once this is done a measurement of the maximum energy deposited by recoiling neutrons can be found. The maximum energy deposited corresponds to neutrons scattering at 180° so we can use Eq. 2.5 to calculate the keVnr of the neutrons and then use that value with the experimental keVee to find the experimental quenching factor.

To determine the back scattered energy we first establish a baseline for the average energy per keV deposited between the neutron signal and the peak caused by the 27 keV EC gammas. Next that baseline is extrapolated back to the neutron signal and the first bin that is 1σ above the baseline is recorded as the max energy deposited. See Fig. 42 for an example of this technique for 1.888 MeV and 1.971 MeV protons.

The values are then compared to the maximum possible energy deposited from a backscattering neutron at the highest energy produced for that proton energy (Eq. 2.5). The uncertainties are those calculated using the statistical error from photoelectrons and the approximate intrinsic resolution of the crystal at that energy added in quadrature. The quenching factors and other pertinent values are listed in Table 4 and plotted in Fig. 43.
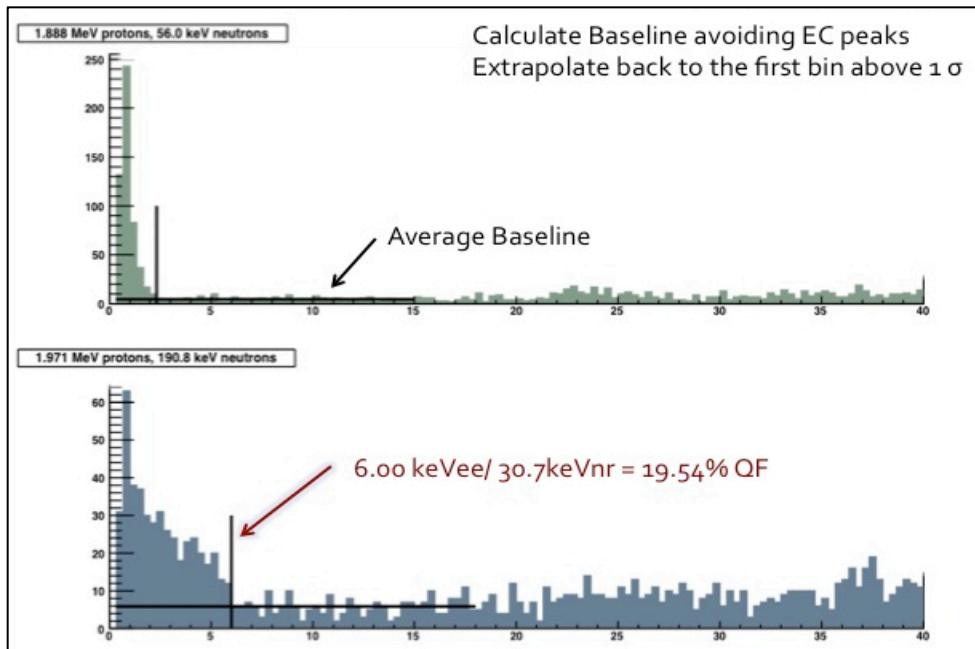

Fig. 42. Energy deposited per event for quenching factor study. Top: 1.888 MeV protons with maximum 56.0 keV neutrons, backscatter energy of 9.02 keVnr. Bottom: 1.971 MeV protons with maximum 190.8 keV neutron, backscatter energy of 30.7 keVnr.

Table 4 Experimental values from quenching factor study. Proton energies range from 1.888 MeV – 2.014 MeV which correspond to neutron backscatter energies from 9.02 keVnr - 39.5 keVnr, Quenching factor values plotted in Fig. 43.

| Values From Quenching Factor Study								
Proton Energy (MeV)	Max Neutron Energy (keV)	Max Recoil Energy (keVnr)	Calculated Baseline (events)	Measured Energy (keVee)	Calculated QF (%)	Approximate Error		
						R_{stat}	R_{np}	R_{tot}
1.888	56.0	9.02	4.57	2.33	25.83	.305	.419	.52
1.901	85.8	13.8	4.73	3.67	26.59	.243	.329	.41
1.915	110.3	17.8	4.80	4.00	22.47	.232	.314	.39
1.929	132.2	21.3	4.73	5.00	23.47	.208	.278	.35
1.943	152.6	24.6	4.50	5.67	23.05	.195	.260	.33
1.957	172.0	27.7	4.76	6.33	22.85	.185	.245	.31
1.971	190.8	30.7	5.86	6.00	19.54	.190	.252	.32
1.985	209.1	33.7	5.16	7.33	21.75	.172	.226	.28
1.999	226.9	36.7	4.80	8.66	23.73	.158	.206	.26
2.014	245.7	39.6	5.30	9.33	23.56	.152	.198	.25
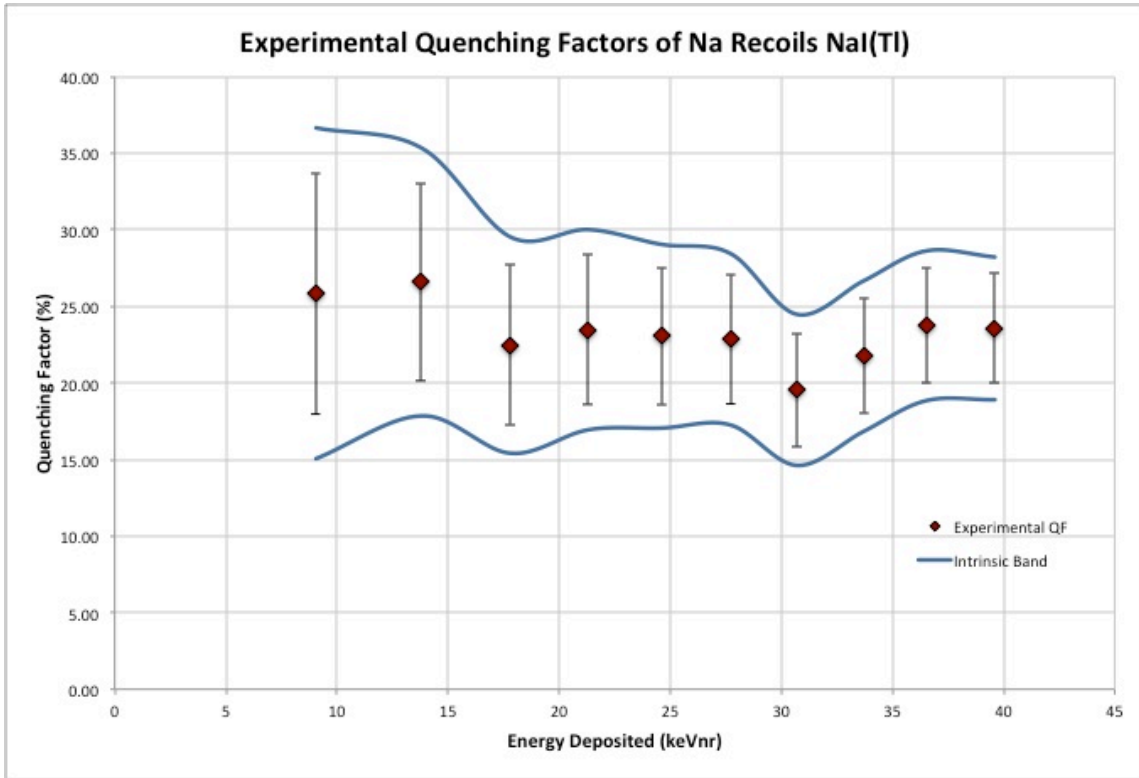
Fig. 43. Experimental results for the quenching factors of sodium nuclear recoils in NaI(Tl) relative to gamma rays of the same energy. Error bars represent the statistical resolution of the crystal. The blue band represents the uncertainty due to the intrinsic resolution of the crystal.

6. CONCLUSIONS

Quenching factors have been measured for the nuclear recoils on sodium across an energy range of 9-39 keVnr using the 180° backscatter edge on our sodium iodide detector. Our results are plotted in Fig. 44 with the published results shown previously in Fig. 27. The values range from 20-27% QF and agree well with other low energy measurements showing no large deviations from expected values. As with other measured QFs for sodium they do not follow the Lindhard prediction curves, Fig. 23. They increase as the energy decreases below 20 keV, just as the results from the Chagani et al. [81]. It is unclear if there is a plateau at that point or if the increase continues below 9 keVnr. Our results also show a dip in the QF values near 30 keV, close to the iodine K-shell absorption edge. This has not been observed in other measurements and warrants further investigation.

Future plans include taking backscatter scintillator coincidence data runs from 5 keV to 40 keV. The NaI(Tl) and paddle counter in coincidence will allow better selection for backscattering events, further reducing background and increasing counting statistics. The hope is to better understand the shape of the curve at these lower energies and reduced the error bars on these data points. Also, several more data sets around 30 keV will be taken to explore the observed dip in QF and determine if it is in fact an actual feature, or just a statistical fluctuation of a smoother distribution.

The search for the missing mass in the Universe has motivated countless scientists in the last 50 years and we continue to search for the elusive WIMP to solve

the question of "What is Dark Matter?" Experiments that use NaI(Tl) crystals rely on accurate characterization and measurements for low energy nuclear interactions in their detectors. Our experiment used a combination of internal radioactive decay gammas and Geant4 simulation to characterize the response of our NaI(Tl) at low energies. The QFs reported show similar values to those previously published. They include interesting features like an increase in low energies and a dip at 30 keV. Future plans will improve and expand on these measurements in order to better understand the response of NaI(Tl) at low energies.
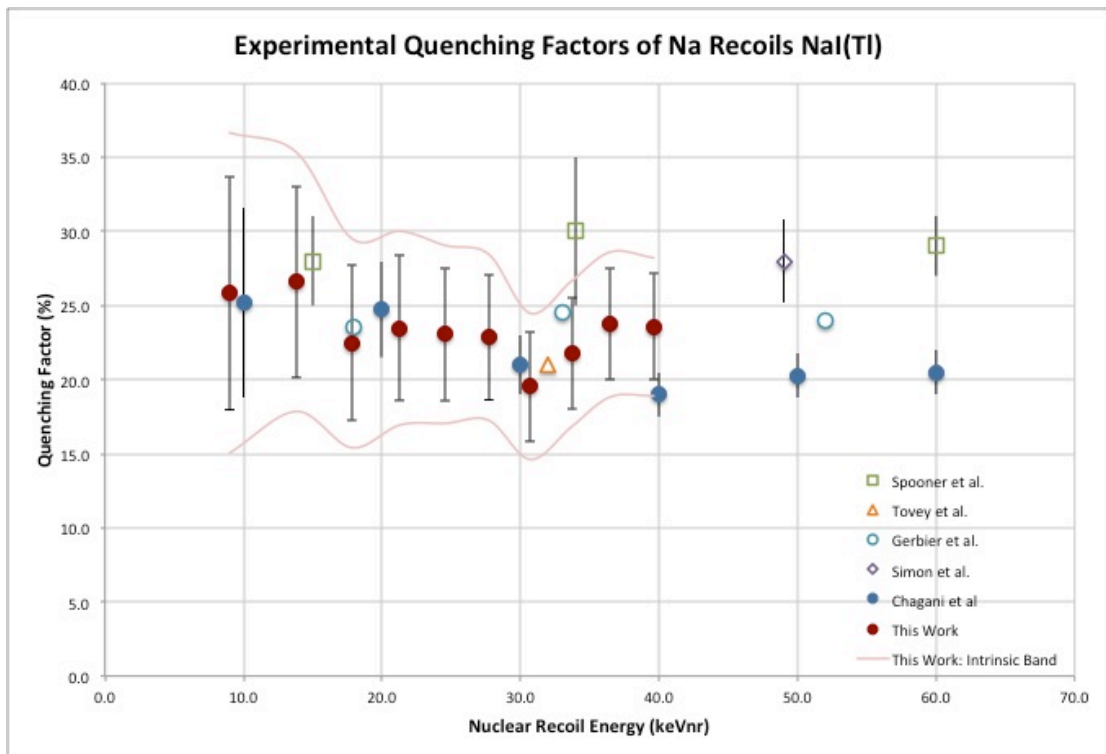

Fig. 44. Results from this experiment plotted with current published measurements of sodium nuclear quenching factors in NaI(Tl) previously shown in Fig. 27.

REFERENCES

[1]   F. Zwicky, Helv. Phys. Acta 6 (1933) 110-127.

[2]   A. Liddle, An Introduction to Modern Cosmology, John Wiley and Sons Inc., West Sussex, England, 2003.

[3]   G. Hinshaw, D. Larson, E. Komatsu, D.N. Spergel, C.L. Bennett, et al., WMAP Collaboration, arXiv:1212.5226v2 [astro-ph.CO] (2012).

[4]   G. Hinshaw, D. Larson, E. Komatsu, D.N. Spergel, C.L. Bennett, et al., WMAP Collaboration, arXiv:1212.5225v2 [astro-ph.CO] (2012).

[5]   S.M. Kent, J.E. Gunn, Astron. J. 87 (7) (1982) 945-971.

[6]   F. Zwicky, Astrophys. J. 86 (3) (1937) 217-246.

[7]   J. Zhao, S. Huang, R. Pan, Y. He, Acta Astrophys. Sin 11 (1991) 119-127.

[8]   M. Girardi, S. Borgani, G. Giuricin, F. Mardirossian, M. Mezzetti, arXiv: astro-ph/9907266v1 (1999).

[9]   R. G. Carlberg, H.K.C. Yee, E. Ellingson, arXiv: astro-ph/9512087v2 (1997).

[10]   H.W. Babcock, Lick Obs. Bull. 498 (1939) 41-51.

[11]   V.C. Rubin, W.K. Ford, Astrphys. J. 159 (1970) 379-403.

[12]   A. Bosma, Astron. J. 86 (12) (1981) 1791-1846.

[13]   M. Persic, P. Salucci, F. Stel, arXiv: astro-ph/9506004v3 (1999).

[14]   P. Salucci, M. Persic, arXiv: astro-ph/9703027v1 (1997).

[15]   M. Roos, Introduction to Cosmology 3rd ed, John Wiley and Sons Inc., West Sussex, England, 2003.

[16]   R. Narayan, arXiv: astro-ph/9606001v2 (1997).

[17]   <http://hubblesite.org/newscenter/archive/releases/2000/07/image/b/> 2011.

[18]   H. Hoekstra, B. Jain, Ann. Rev. Nucl. Part. Sci. 58 (2008) 99-123. [arXiv: 0805.0139v1 [astro-ph]].

[19]   M. Bartelmann, P. Schneider, Phys. Rept. 340 (2001) 291-472. [arXiv: astro-ph/9912508v1].

[20]   D. Clowe, M. Bradac, A.H. Gonzalez, M. Markevitch, S.W. Randall, et al., Astrophys. J. 648 (2006) 109-113. [arXiv: astro-ph/0608407v1].

[21]   < http://hubblesite.org/newscenter/archive/releases/exotic/dark%20matter/ 2012/10/image/b/ > 2012.

[22]   S. Perlmutter, B.P. Schmidt, Lect. Notes. Phys. 598 (2003) 195-217. [arXiv: astro-ph/0303428v1]

[23]   S.W. Barwick, J.F. Beacom, V. Cianciolo, S. Dodelson, J.L. Feng et al., arXiv: astro-ph/0412544v1 (2004).

[24]   M. Kowalski, D. Rubin, G. Aldering, R.J. Agostinho, A. Amadon, et al., Astrophys. J. 686 (2008) 749-778. [arXiv: 0804.4142v1 [astro-ph]].

[25]   A.A. Penzias, R.W. Wilson, Astrophys. J. 142 (1965) 419-421.

[26]   E. Komatsu, K.M. Smith, J. Dunkley, C.L. Bennett, B. Gold, et al., WMAP Collaboration, Astrophys. J. Suppl. 192 (2011) 18-65. [arXiv: 1001.4538v3 [astro-ph.CO]].

[27]   W. Hu, N. Sugiyama, J. Silk, Nature 386 (1997) 37-43. [arXiv: astro-ph/9604166v1].

[28]   C.L. Bennett, M. Halpern, G. Hinshaw, N. Jarosik, A. Kogut, et al., WMAP Collaboration, Astrophys. J. Suppl. 148 (2003) 1-43. [arXiv: astro-ph/0302207v3].

[29]   K. A. Olive, arXiv: astro-ph/ 0301505v2 (2003).

[30]   P.A.R. Ade, N. Aghanin, C. Armitage-Caplan, M. Arnaud, M. Ashdown, et al., Plank Collaboration, arXiv: 1303.5062v1 (2013).

[31]   C.L. Reichardt, P.A.R. Ade, J.J. Bock, J.R. Bond, J.A. Brevik, et al., Astrophys. J. 694 (2009) 1200-1219. [arXiv: 0801.1491v3].

[32]   M.L. Brown, P.A.R. Ade, J.J. Bock, M. Bowden, G. Cahill, et al., QUaD Collaboration, Astrophys. J. 705 (2009) 978-999.

[33]   W. Hu, S. Dodelson, Annu. Rev. Astro. Astrophys. 40 (2002) 171-216.

[34] P.A.R. Ade, N. Aghanin, C. Armitage-Caplan, M. Arnaud, M. Ashdown, et al., Plank Collaboration, arXiv: 1303.5076v1 (2013).

[35] J.A. Peacock, S. Cole, P. Norberg, C.M. Baugh, J. Bland-Hawthorn, et al., Nature 410 (2001) 169-173.

[36] M. Tegmark, D.J. Eisenstein, M.A. Strauss, D.H. Weinberg, M.R. Blanton, et al., Phys. Rev.D 74 (2006) 123507. [arXiv: astro-ph/0608632].

[37] < http://www.sdss.org/includes/sideimages/sdss_pie2.html >

[38] D.J. Eisenstein, I. Zehavi, D.W. Hogg, R. Scoccimarro, R.C. Nichol, et al., Astrophys. J. 633 (2005) 560-574. [arXiv: astro-ph/0501171v1].

[39] G.R. Blumenthal, S.M. Faber, J.R. Primack, M.J. Rees, Nature 311 (1984) 517-525.

[40] R.A. Alpher, H. Bethe, G. Gamow, Phys. Rev. 73 (7) (1948) 803-804.

[41] G. Steigman, arXiv: astro-ph/0307244v1 (2003).

[42] G. Steigman, Annu. Rev. Nucl. Part. Sci. 57 (2007) 463-491.

[43] J. Beringer, J.F. Arguin, R.M. Barnett, K. Copic, O. Dahl, et al., Particle Data Group, Phys. Rev. D 86 (010001) (2012).

[44] J. M. O'Meara, S. Burles, J.X. Prochaska, G.E. Prochter, R.A. Bernstein, et al., Astrophys. J. 649 (2006) 61-66. [arXiv: astro-ph/0608302v1].

[45] R.H. Cybert, B.D. Fields, K.A. Olive, Astroparticle Physics 23 (2005) 313-323.

[46] R.H. Cybert, B.D. Fields, K.A. Olive, arXiv: 0808.2818v1 [astro-ph] (2008).

[47] L. Roszkowski, Pramana 62 (2) (2004) 389-401. [arXiv: hep-ph/0404052v1].

[48] G. Bertone, D. Hoope, J. Silk, Phys. Rept. 405 (2005) 279-390. [arXiv: hep-ph/0404175v2].

[49] P.J.E. Peebles, Science 224 (4656) (1984) 1385-1391.

[50] S. Weinberg, Phys. Rev. Lett. 40 (2) (1978) 223-226.

[51] R.J. Gaitskell, Annu. Rev. Nucl. Part. Sci. 54 (2004) 315-359.

[52]   S.J. Asztalos, L.J. Rosenberg, K van Bibber, P. Sikivis, K. Zioutas, et al., Annu. Rev. Nucl. Part. Sci. 56 (2006) 293-326.

[53]   R. Battesti, B. Beltran, H. Davoudiasl, M. Kuster, P. Pugnat, Lect. Notes Phys. 741 (2008) 199-237. [arXiv: 0705.0615v1 [hep-ex]].

[54]   S. Andriamonje, S. Aune, D. Autiero, K. Barth, A. Belov, et al., CAST Collaboration, arXiv: hep-ex/0702006v3.

[55]   E. Zavattini, G. Zavattini, G. Ruoso, E. Polacco, E. Milotti, et al., PVLAS Collaboration, Phys. Rev. Lett. 96 (2006) 110406.

[56]   E. Zavattini, G. Zavattini, G. Raiteri, G. Ruoso, E. Polacco, et al., PVLAS Collaboration, Phys. Rev. D 77 (2008) 032006.

[57]   G. Jungman, M. Kamionkowski, K. Griest, Phys. Rept. 267 (1996) 195-373.

[58]   M.C. Smith, G.R. Ruchti, A. Helmi, R.F.G. Wyse, J.P. Fulbright, et al., Mon. Not. R. Astron. Soc. 379 (2007) 755-772.

[59]   J.D. Lewin, P.F. Smith, Astroparticle Phys. 6 (1996) 87-112.

[60]   J. Engel, Phys. Lett. B 264 (1991) 114-119.

[61]   J. Engel, S. Pittel, P. Vogel, Int. J. Mod. Phys. E 1 (1992) 1-37.

[62]   R.H. Helm, Phys. Rev. 104 (5) (1956) 1466-1475.

[63]   G. Fricke, C. Bernhardt, K. Heilig, L.A. Schaller, L. Schellenberg, et al., Atomic Nuclear Data and Data Tables 60 (1995) 177-285.

[64]   R.Bernabei, P. Belli, F. Cappella, R. Cerulli, C.J. Dai, et al., Eur. Phys. J. C 56 (2008) 333-355. [arXiv: 0804.2741v1 [astro-ph]].

[65]   R.Bernabei, P. Belli, F. Cappella, R. Cerulli, C.J. Dai, et al., Eur. Phys. J. C 67 (2010) 39-49. [arXiv: 1002.1028v1 [astro-ph.GA]].

[66]   C.E. Aalseth, P.S. Barbeau, N.S. Bowden, B. Cabrera-Palmer, J. Colaresi, et al., Phys. Rev. Lett. 106 (2011) 131301. [arXiv: 1002.4703v2 [astro-ph.CO]].

[67]   C.E. Aalseth, P.S. Barbeau, J. Colaresi, J.I. Collar, J. Diaz Leon, et al., Phys. Rev. Lett. 107 (2011) 141301. [arXiv: 1106.0650v3 [astro-ph.CO]].

[68]   G. Angloher, M. Bauer, I. Bavykina, A. Bento, C. Bucci, et al., arXiv: 1109.0702v1 [astro-ph.CO] (2011).

[69]   R. Agnese, Z. Ahmed, A.J. Anderson, S. Arrenberg, D. Balakishiyeva, et al., CDMS Collaboration, arXiv: 1304.3706v2 [astro-ph.CO] (2013).

[70]   E. Aprile, K. Arisaka, F. Arneodo, A. Askin, L. Baudis, et al., Xenon100 Collaboration, Astropart. Phys. 35 (2012) 573-590. [arXiv: 1107.2155v2 [astro-ph.IM]].

[71]   A.S. Torrento-Coello, arXiv: 1106.1454v1 [hep-ex] (2011).

[72]   R. Agnese, Z. Ahmed, A.J. Anderson, S. Arrenberg, D. Balakishiyeva, et al., CDMS Collaboration, arXiv: 1304.4279v2 [hep-ex] (2013).

[73]   G.J. Alner, H.M. Araújo, G.J. Arnison, J.C. Barton, A. Bewick, et al., UK Dark Matter Collaboration, Phys. Lett. B 616 (2005) 17-24.

[74]   K. Fushimi, H. Ejiri, K. Hayashi, R. Hazama, T. Kishimoto, et al., Astroparticle Phys. 12 (1999) 185-192.

[75]   J. Amaré, B. Beltrán, J. M. Carmona, S. Cebrián, E. García, et al., J. Phys.: Conf. Ser. 39 (2006) 123-125.

[76]   J. Lindhard, V. Nielsen, M. Scharff, P.V. Thomsen, Mat. Fys. Medd. Dan. Vid. Selsk. 33 (10) (1963) 1-42.

[77]   J. Lindhard, M. Scharff, H.E. Schiøtt, Mat. Fys. Medd. Dan. Vid. Selsk. 33 (14) (1963) 1-42.

[78]   A. Hitachi, in: Proc. Int. Workshop IDM'2006, 11-16 September 2006, Rhodes, Greece, p. 344-349.

[79]   J.B. Birks, The Theory and Practice of Scintillation Counting, Pergamon Press, Oxford, 1964.

[80]   D.R. Tovey, V. Kudryavtsev, M. Lehner, J.E. McMillan, C.D. Peak, et al., Phys. Lett. B 433 (1998) 150-155.

[81]   H. Chagani, P. Majewski, E.J. Daw, V.A. Kudryavtsev, N.J.C. Spooner, Journal of Instrumentation 3 (2008) P06003.

[82]   V.I. Tretyak, Astropart. Phys. 33 (2010) 40-53.

[83]   D. Engelkemeir, Rev. Sci. Instr. 27 (8) (1956) 589-591.

[84]   P. Iredale, Nucl. Instr. Meth. 11 (1961) 336-339.

[85]   P. Iredale, Nucl. Instr. Meth. 11 (1961) 340-346.

[86]   C.D. Zerby, A. Meyer, R.B. Murray, Nucl. Instr. Meth. 12 (1961) 115-123.

[87]   J.D. Valentine, B.D. Rooney, J. Li, IEEE Trans. Nucl. Sci. 45 (3) (1998) 512-517.

[88]   B.D. Rooney, J.D. Valentine, IEEE Trans. Nucl. Sci. 44 (3) (1997) 509-516.

[89]   M. Moszyński, M. Kapusta, M. Mayhugh, D. Wolski, S.O. Flyokt, IEEE Trans. Nucl. Sci. 44 (3) (1997) 1052-1061.

[90]   M. Moszyński, J. Zalipska, M. Balcerzyk. M. Kapusta, W. Mengesha, et al., Nucl. Instr. Meth. A 484 (2002) 259-269.

[91]   I.V. Khodyuk, P.A. Rodnyi, P. Dorenbos, J. Appl. Phys. 107 (2010) 113513. [arXiv: 1102.3799v1 [physics.ins-det]].

[92]   G. Gerbier, J. Mallet, L. Mosca, C. Tao, B. Chambon, et al., Astropart. Phys. 11 (1999) 287-302.

[93]   N.J.C. Spooner, G.J. Davies, J.D. Davies, G. J. Pyle, T.D. Bueknell, et al., Phys. Lett. B 321 (1994) 156-160.

[94]   E. Simon, L. Bergé, A. Broniatowski, R. Bouvier, B. Chambon, et al., Nucl. Intr. Meth. A 507 (2003) 643-656.

[95]   R.E. White, P.H. Barker, D.M.J. Lovelock, Metrologia 21 (1985) 193-199.

[96]   C.A. Bertulani, Nuclear in Physics in a Nutshell, Princeton University Press, Princeton, NJ, 2007.

[97]   D.M. Mattox, Handbook of Physical Vapor Deposition (PVD) Processing 2nd ed., doi: 10.1016/B978-0-8155-2037-5.00015-0, (2007).

[98]   S. Agostinelli, J. Allison, K. Amako, J. Apostolakis, H. Araujo, et al., Nucl. Instr. Meth. A 506 (2003) 250-303. < http://geant4.cern.ch >.

[99]   < http://ie.lbl.gov/toi/nuclide.asp?iZA=530128 >

[100] Ł. Świderski, M. Moszyński, W. Czarnacki, A. Syntfeld-Każuch, IEEE Nuclear
Science Symposium Conference (2) (2006) 1122-1128.

[101] R. Brun, F. Rademakers, Nucl. Instr. Meth. A 389 (1997) 81-86.
< http://root.cern.ch >